Title	A comprehensive iso-octane combustion model with improved thermochemistry and chemical kinetics
Author(s)	Atef, Nour; Kukkadapu, Goutham; Mohamed, Samah Y.; Al Rashidi, Mariam J.; Al Rashidi, Mariam; Banyon, Colin; Mehl, Marco; Heufer, Karl Alexander; Nasir, Ehson F.; Alfazazi, A.; Das, Apurba K.; Westbrook, Charles K.; Pitz, William J.; Lu, Tianfeng; Farooq, Aamir; Sung, Chih-Jen; Curran, Henry J.; Sarathy, S. Mani
Publication Date	2017-02-05
Publication Information	Atef, N,Kukkadapu, G,Mohamed, SY,Al Rashidi, M,Banyon, C,Mehl, M,Heufer, KA,Nasir, EF,Alfazazi, A,Das, AK,Westbrook, CK,Pitz, WJ,Lu, TF,Farooq, A,Sun, CJ,Curran, HJ,Sarathy, SM (2017) 'A comprehensive iso-octane combustion model with improved thermochemistry and chemical kinetics'. Combustion And Flame, 178 :111-134. doi: https://doi.org/10.1016/j.combustflame.2016.12.029
Publisher	Elsevier
Link to publisher's version	http://dx.doi.org/10.1016/j.combustflame.2016.12.029
Item record	http://hdl.handle.net/10379/6872
DOI	http://dx.doi.org/10.1016/j.combustflame.2016.12.029

A comprehensive iso-octane combustion model with improved thermochemistry and chemical kinetics

Nour Atef[a*], Goutham Kukkadapu[b], Samah Y. Mohamed[a], Mariam Al Rashidi[a], Colin Banyon[c], Marco Mehl[d], Karl Alexander Heufer[c], Ehson F. Nasir[a], A. Alfazazi[a], Apurba K. Das[b], Charles K. Westbrook[d], William J. Pitz[d], Tianfeng Lu[e], Aamir Farooq[a], Chih-Jen Sung[b], Henry J. Curran[c], S. Mani Sarathy[a*]

[a] King Abdullah University of Science and Technology (KAUST), Clean Combustion Research Center (CCRC), Thuwal 23955-6900, Saudi Arabia
[b] Department of Mechanical Engineering, University of Connecticut, Storrs, CT, United States
[c] Combustion Chemistry Centre, Ryan Institute, School of Chemistry, National University of Ireland, Galway, Ireland
[d] Lawrence Livermore National Laboratory, Livermore, CA, United States
[e] Department of Mechanical Engineering, University of Connecticut, Storrs, CT 06269-3139, USA

**Corresponding Authors:*

Nour Atef

Nour.atef@kaust.edu.sa

S. Mani Sarathy

Mani.sarathy@kaust.edu.sa

Al Kindi Building 5 Room 4336

KAUST

Thuwal, Saudi Arabia 23955

Abstract

iso-Octane (2,2,4-trimethylpentane) is a primary reference fuel and an important component of gasoline fuels. Moreover, it is a key component used in surrogates to study the ignition and burning characteristics of gasoline fuels. This paper presents an updated chemical kinetic model for iso-octane combustion. Specifically, the thermodynamic data and reaction kinetics of iso-octane have been re-assessed based on new thermodynamic group values and recently evaluated

rate coefficients from the literature. The adopted rate coefficients were either experimentally measured or determined by analogy to theoretically calculated values. Furthermore, new alternative isomerization pathways for peroxy-alkyl hydroperoxide (ȮOQOOH) radicals were added to the reaction mechanism. The updated kinetic model was compared against new ignition delay data measured in rapid compression machines (RCM) and a high-pressure shock tube. These experiments were conducted at pressures of 20 and 40 atm, at equivalence ratios of 0.4 and 1.0, and at temperatures in the range of 632–1060 K. The updated model was further compared against shock tube ignition delay times, jet-stirred reactor oxidation speciation data, premixed laminar flame speeds, counterflow diffusion flame ignition , and shock tube pyrolysis speciation data available in the literature. Finally, the updated model was used to investigate the importance of alternative isomerization pathways in the low temperature oxidation of highly branched alkanes. When compared to available models in the literature, the present model represents the current state-of-the-art in fundamental thermochemistry and reaction kinetics of iso-octane; and thus provides the best prediction of wide ranging experimental data and fundamental insights into iso-octane combustion chemistry.

Keywords: iso-Octane ,combustion kinetics, thermodynamics, gauche, alternative isomerisation

1- Introduction

A better understanding of fuel oxidation chemistry and kinetics is crucial for improving the design of modern internal combustion engines (ICE) [1]. For example, end-gas autoignition (i.e., knock) in spark ignition (SI) engines and combustion phasing in homogeneous charge compression ignition engines (HCCI) and partially premixed combustion (PPC) engines are driven by chemical kinetic processes [2-4]. A thoroughly tested kinetic model enables the accurate simulation of engine experiments and gives insight into the effect of fuel composition on HCCI engine combustion phasing [5]. Iso-octane (2,2,4-trimethylpentane) is a gasoline primary reference fuel (PRF) that is highly knock resistant, with an assigned octane number of 100. Since PRF mixtures may be used as surrogates of gasoline, their kinetics and ignition properties have been extensively investigated over the past few decades, both experimentally and theoretically. Most pratical gasoline fuels have octane numbers above 85, and therefore iso-

octane is the principal component in PRF surrogates and strongly governs their combustion chemistry.

Various fundamental combustion experiments have been conducted for iso-octane, including ignition delay time and pyrolysis measurements in shock tubes [6-12] and rapid compression machines (RCM) [13-20], premixed laminar flame speed measurements [21-29], and ignition temperature measurements in counterflow flames [30, 31]. However, the majority of experiments were conducted at relatively high temperatures because iso-octane is generally less reactive at lower temperatures (i.e., compared to normal alkanes such as *n*-heptane). The measurement of intermediate species for iso-octane low temperature oxidation is limited to the measurement of species' concentration profiles in a jet-stirred reactor (JSR) [32-34] using gas chromatography and mass spectrometry.

A comprehensive chemical kinetic model for iso-octane was presented by Curran et al. [35]. The model was developed based on the low- and high-temperature reaction pathways and rate rules proposed earlier for the Lawrence Livermore National Laboratory (LLNL) *n*-heptane model [36]; however, some modifications were made to better predict experimental iso-octane reactivity. The model was compared against various experimental data sets and showed good agreement. Later, Mehl et al. [1, 37] further developed the low temperature reaction mechanism for iso-octane oxidation to better predict low temperature heat release (LTHR) in HCCI engines. Although both versions of the model are capable of matching a wide range of experimental data sets available in the literature, there have been some experimental data sets that are difficult to match, in particular, shock tube ignition data [9] and HCCI LTHR profiles of PRF mixtures containing a large amount of iso-octane (i.e., PRF 85–100) [37-40]. The aforementioned studies [9, 37-40] indicate that the currently available iso-octane kinetic models are not sufficiently reactive at low and intermediate temperatures and lean conditions encountered in HCCI engines. Experimental data of iso-octane ignition at 600-800 K and lean conditions are needed to further improve the model.

Since the publication of the latest comprehensive iso-octane model [1], several computational studies have been reported for iso-octane thermochemistry and kinetics. Snitsiriwat and Bozzelli [41] computed the standard heat of formation, entropy, and specific heat capacities of iso-octane and its radicals at the CBS-QB3//B3LYP/6-31G(d,p) level of theory. Later, Auzmendi-Murua

and Bozzelli [42] performed energy calculations on the potential energy surface of the secondary iso-octyl radical + O_2 system at the CBS-QB3//B3LYP/6-31G(d,p) level of theory, and provided corresponding thermochemical and kinetic data. Recently, the thermochemistry of species and kinetics of reactions lying on the potential energy surface of tertiary iso-octyl + O_2 system were computationally studied at the CBS-QB3//B3LYP/6-31G(d,p) level of theory [43]. Finally, the pressure-dependent kinetics of iso-octane unimolecular decomposition, radical β-scission, and radical isomerization were computed using the CASPT2-(2e,2o)/6-31+G(d,p)//CAS(2e,2o)/6-31+G(d,p) level of theory and Rice−Ramsperger−Kassel−Marcus/Master Equation (RRKM/ME) analysis [44].

In addition, several computational studies [45-48] have been recently reported regarding the low-temperature oxidation kinetics of normal and branched alkanes. The calculated rate coefficients have been implemented in the oxidation mechanisms of three pentane isomers (i.e., *n*-pentane, iso-pentane and neo-pentane) [49], *n*-hexane [50], and 2-methylhexane [51]. The use of these coefficients and the addition of alternative peroxy-alkyl hydroperoxide (ȮOQOOH) isomerization pathways were found to improve the agreement between simulated and experimental ignition delay data for the fuels considered.

In the present work, a comprehensive approach is taken to update the iso-octane detailed chemical kinetic model developed by Curran et al. [35] and Mehl et al. [1]. Specifically, we updated thermochemistry group values and reaction rate coefficients based on new experimental or theoretical studies. We also incorporated alternative isomerization pathways for peroxy-alkylhydroperoxide species (ȮOQOOH) and third O_2 addition pathways suggested by Wang et al. [52, 53]. The updated model was compared against new RCM ignition delay data from three different facilities at King Abdullah University of Science and Technology (KAUST), National University of Ireland Galway (NUIG), and University of Connecticut (UCONN). The conditions covered by these facilities were low and intermediate temperatures (632–1060K), equivalence ratios of 1 and 0.4, and nominal pressures of 20 and 40 atm. In addition, new high-pressure shock tube ignition delay data at 20 atm from KAUST were obtained. The updated model was also tested against data of ignition delay times [6-9], JSR oxidation speciation data [32], premixed laminar flame speeds [21, 23-26, 28, 29], counterflow flame ignition data [54], and

shock tube pyrolysis speciation data [12] available in the literature. Chemical kinetic mechanism reduction was utilized to generate a skeletal mechanism that was used in flame simulations.

2- Chemical kinetic modeling

The updated comprehensive chemical kinetic model for iso-octane was developed by jointly researchers at KAUST, LLNL, NUIG, and UCONN. The thermochemical data for all species in the iso-octane sub-mechanism were updated using new group values and detailed analysis of intra-molecular interactions. Our updated thermochemistry was compared to literature data available for a limited number of species that have been subject to high-level theoretical calculations. The chemical kinetic reaction mechanism was also updated with new reaction classes and rate rules. Further details about the thermochemistry and reaction mechanism are provided in the following sections.

2-1 Thermochemistry

Chemical kinetic models require thermochemical data, not only for calculating the mixture temperature, but also for calculating the rates of reversible reactions. In this work, we re-evaluated the thermochemical data of all species involved in the iso-octane oxidation sub-mechanism using Benson's group additivity method [55], as implemented in THERM software [56].

The new group values suggested by Burke et al. [57] and Simmie and Somers [58] were used, and gauche interactions were accounted for based on the work of Sabbe et al. [59]. Iso-octane is a highly branched molecule that has three full alkane gauche (AG) interactions according to the Newman projection shown in Fig. 1a and 1b. Each gauche interaction is estimated to add 0.8 kcal to the heat of formation of the molecule [60]. In the case of iso-octyl radicals, the contribution of the gauche interaction to the heat of formation depends on the nature of the radical site. In their work, Sabbe et al. [59] distinguished between two different types of gauche interactions for radicals: i) interaction between two *sp3*-hybridized carbon groups, one of which is connected to the radical site (RG1), and ii) interaction between an *sp2*-hybridized and an *sp3*-hybridized carbon groups (RG2). According to the calculations performed by [59], RG1 and RG2 interactions are 40% and 76% lower in energy than a full gauche interaction, respectively. For implementation in the THERM program, the total gauche interactions for each radical were

rounded off to a total number of whole gauche interactions. Therefore, only two gauche interactions are considered for primary iso-octyl radicals ($A\dot{C}_8H_{17}$ and $D\dot{C}_8H_{17}$) and 3 gauche interactions for secondary and tertiary iso-octyl radicals ($B\dot{C}_8H_{17}$ and $C\dot{C}_8H_{17}$) (refer to the Supplementary material for species nomenclature). For cyclic ethers, gauche interactions are only considered if one or both of the interacting groups are not within the cycle, as shown in Fig. 1e and 1f. This methodology was tested by comparing standard enthalpy of formation and entropies from THERM and those from computational chemistry as discussed below.

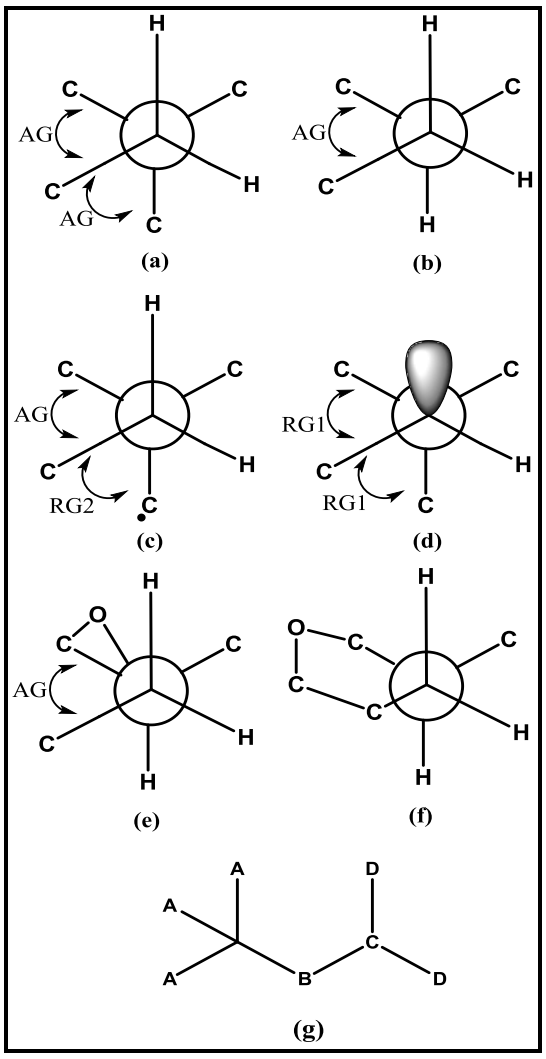

Figure 1. Newman projections showing gauche interactions for the iso-octane molecule along (a) secondary-quaternary bond and (b) secondary-tertiary bond; radical interactions (c) RG2, (d) RG1, and (e,f) cyclic ethers; and (g) structure of iso-octane with site labels.

Based on the methodology proposed by [59] for olefinic species, gauche interactions between an *sp3*-hybridized carbon center and an *sp2*-hybridized one, such as the interaction between C1 and C6 in 2,2,4 trimethyl-pent-3-ene (Fig. 2a), were not included because they are already accounted for in other group values. For example, the C/C3/CD group used for the quaternary carbon center in 2,2,4 trimethyl-pent-3-ene includes the interaction between groups 1 and 6.

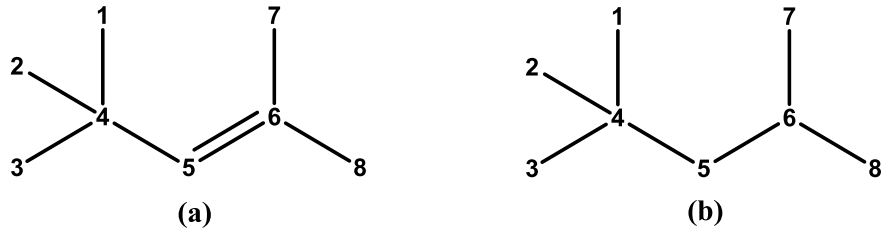

Figure 2. 2,2,4 trimethyl-pent-3-ene (a) and iso-Octane (b)

Another destabilizing interaction in the iso-octane molecule is the 1,5 hydrogen interaction resulting from the repulsion between the two methyl groups lying on the same side of the molecule (e.g., C1 and C7 in the carbon skeletal Fig. 2b). This adds 1.5 kcal mol^{-1} to the heat of formation as reported by Benson et al. [60]. This destabilizing effect is lower in the case of radicals, as reported by Sabbe et al. [59], especially for the tertiary iso-octyl radical (-0.43 kcal mol^{-1}). When calculating the thermodynamic properties of radicals, standard THERM hydrogen interaction groups were used; the number of standard groups included was chosen to most closely match the specific radical hydrogen interactions. Thus, the 1,5 hydrogen interaction in our group additivity thermochemistry estimation for the tertiary iso-octyl radical (-0.43 kcal mol^{-1}) is neglected.

In addition to gauche and 1,5 hydrogen interactions, we added an optical isomer group (OI) for every chiral center and hydroperoxy OOH functional group (pseudo-chiral center). This adds R×ln 2 to the entropy of the species, which affects the equilibrium constant:

$$K_{eq} = \frac{k_f}{k_b} = \exp(\frac{-\Delta H}{RT} + \frac{\Delta S}{R})$$

where K_{eq} is the equilibrium constant, k_f and k_b are rates of forward and backward reactions respectively, ΔH and ΔS are the change in the enthalpy and entropy of chemical reaction.

Computational standard heat of formation values of iso-octane [41], iso-octyl radicals [41], and species involved in the potential energy surfaces of secondary [42] and tertiary iso-octyl radical + O_2 [43] are available in the literature. These values, calculated at the CBS-QB3 level of theory, were compared to those calculated using group additivity, as shown in Table 1. The agreement between the two sets of values is within the uncertainty limits of the computational values (± 1.5–2.0 kcal mol^{-1}), except for species with an OOH group attached to the tertiary site and for four membered ring cyclic ethers. The differences observed for these species are likely due to uncertainties in the magnitudes of the gauche and 1,5 hydrogen interactions. To correct for such systematic discrepancies, we applied a +2 kcal mol^{-1} correction to the heat of formation of all species with a tertiary OOH group and a –4 kcal mol^{-1} correction to the heat of formation of all four membered ring cyclic ethers. These corrections did not affect simulated ignition delay times or jet stirred reactor species profiles (comparison shown in Fig. S1 of the Supplementary material). High-level quantum chemical calculations with uncertainties of less than 1 kcal mol^{-1} are needed to develop a rigorous set of group values and counting schemes that allow for more accurate estimation of thermochemical properties of complex species. A comparison between calculated and estimated entropy values of various species is presented as Supplementary material (Table S2) along with a species dictionary and the input groups employed in THERM (Table S1).

Table 1. Comparison of calculated [41-43] and THERM estimated heats of formation of different species. Species that exhibit large discrepancies are shown in bold. All values in kcal mol^{-1}.

		Calculated [41-43]	Estimated using THERM	Difference	Corrected	Difference after correction	Applied Correction
Fuel and fuel radicals	IC8H18	−54.40 ± 1.60	−53.14	1.26			
	$AC\dot{8}H_{17}$	−5.00 ± 1.69	−4.89	0.11			
	$BC\dot{8}H_{17}$	−9.03 ± 1.84	−7.17	1.86			
	$CC\dot{8}H_{17}$	−12.30 ± 2.02	−10.22	0.06			
	$DC\dot{8}H_{17}$	−5.18 ± 1.69	−4.89	0.29			
ROOH,QOOH, RO2	$BC_8H_{17}OOH$	−75.47	−75.77	−0.30			
	$BC_8H_{17}\dot{O}_2$	−42.75	−42.60	0.15			
	$BC\dot{8}H_{16}OOH$-A	−26.30	−27.52	−1.22			
	$BC\dot{8}H_{16}OOH$-C	−31.00	−31.35	−0.35			

	$B\dot{C}_8H_{16}OOH$-D	−26.88	−27.52	−0.64			
	$CC_8H_{17}OOH$	**−77.85**	**−80.10**	**−2.25**	**−78.10**	**−0.25**	**(+2)**
	$CC_8H_{17}\dot{O}_2$	−45.80	−46.93	−1.13			
	$C\dot{C}_8H_{16}OOH$-B	**−31.90**	**−34.13**	**−2.23**	**−32.13**	**−0.23**	**(+2)**
	$C\dot{C}_8H_{16}OOH$-D	**−28.50**	**−31.85**	**−3.35**	**−29.85**	**−1.35**	**(+2)**
	$C\dot{C}_8H_{16}OOH$-A	**−29.70**	**-31.85**	**−2.15**	**−29.85**	**−0.15**	**(+2)**
Cyclic ethers	IC8ETERCD	−55.12	−54.17	0.95			
	IC8ETERAC	−76.82	−76.74	0.08			
	IC8ETERAB	**−57.42**	**−53.44**	**3.98**	**−57.44**	**−0.02**	**(−4)**
	IC8ETERBC	−58.72	−58.20	0.52			
	IC8ETERBD	**−58.32**	**−53.44**	**4.88**	**−57.44**	**0.88**	**(−4)**
Alkoxy	$BC_8H_{17}\dot{O}$	−38.30	−40.46	−2.16			
radicals	$CC_8H_{17}\dot{O}$	−45.50	−42.93	2.57			

2-2 Chemical kinetic mechanism

The updated iso-octane oxidation sub-mechanism was built upon that of H_2 and C_1–C_7 hydrocarbons in a hierarchical manner. AramcoMech 2.0 [61] was used for the C_0–C_4 base chemistry, whereas the chemistry of C_5–C_7 species was taken from LLNL's gasoline surrogate mechanism [1], with the addition of the mechanism by Metcalfe et al. [62] for the di-isobutylene isomers that are produced from iso-octane's alkylperoxy radicals ($RO\dot{O}$) by concerted $H\dot{O}_2$ radical elimination reactions and C-H β-scission of the iso-octyl radicals. The original high- and low-temperature chemistry of iso-octane was taken from [1], and the rate coefficients for nine reaction classes associated with low-temperature kinetics were updated. The updated classes are shown in Fig. 3. These include H-atom abstraction by $\dot{O}H$ radicals, alkyl radical addition to O_2, concerted elimination of $H\dot{O}_2$ radicals from alkylperoxy radicals, alkylperoxy/hydroperoxy alkyl isomerization, formation of cyclic ethers, β-scission reactions of hydroperoxy alkyl radicals, QOOH radical addition to O_2, and isomerization of $\dot{O}OQOOH$ species. Alternative isomerizations, concerted eliminations, hydrogen-exchange and third O_2 addition pathways for peroxy-alkyl hydroperoxide ($\dot{O}OQOOH$) radicals were also added to the mechanism. Since the kinetics of these reactions has never been studied before, their rate coefficients were estimated by analogy. The complete updated mechanism consists of 9220 reactions and 2768 species, with 481 reactions and 179 species specific to the iso-octane sub-mechanism.

For all pressure-dependent low temperature oxidation reactions, only the high pressure limit rates were included following the recommendations of Villano et al. [46]. They conducted simulations for n-butyl radical + O_2 using two mechanisms; one including pressure dependent rate coefficients and another using only the high pressure limit rates. The authors concluded that the high pressure limit for RO_2 and QOOH reactions are sufficient under conditions relevant to practical combustors (i.e., pressures higher than a few atmospheres). They also showed that RO_2 radicals are collisionally stabilized at elevated pressure conditions, which results in well-skipping $R+O_2$ reactions to form alkenes+HO_2 and cyclic ethers+OH being less important. Simulations of low temperature oxidation below one atmosphere may require pressure-dependent rate coefficients, but such conditions less relevant to practical engines.

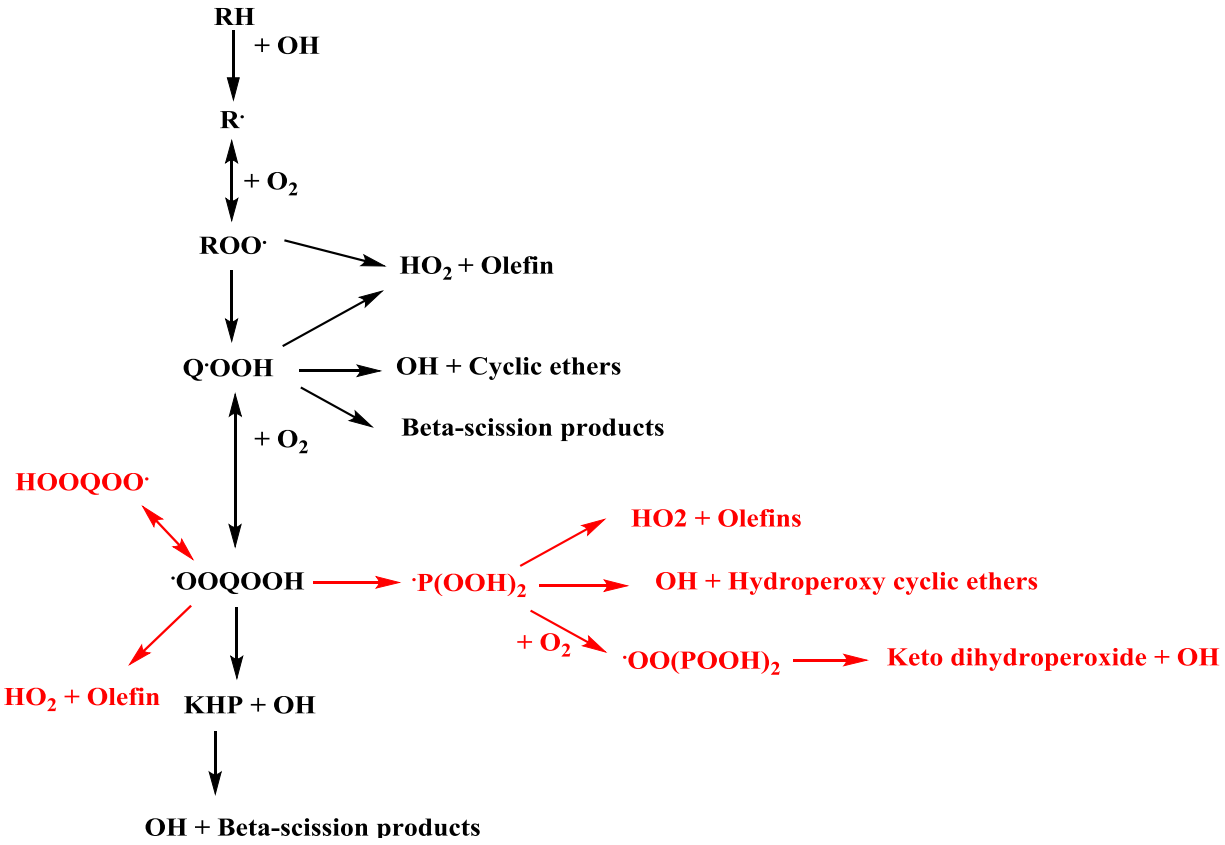

Figure 3. Reaction classes for which rate coefficients were updated. The newly added pathways are shown in red.

2-2-1 Hydrogen abstraction reactions

In this work, the rate coefficients of all H-atom abstraction reactions were updated based on the rate rules suggested by Sarathy et al. [63], except for H-atom abstraction by ȮH radicals, for which experimentally-derived rate rules were recently made available [64, 65]. Sivaramakrishnan and co-workers [64] provided rate rules that were inferred from shock tube kinetic measurements of H-atom abstraction by ȮH radicals from five saturated hydrocarbons comprising different types of abstraction sites (primary, secondary and tertiary). The next-nearest-neighbor (NNN) effects, discussed by Cohen [66], were accounted for, and abstraction sites were further distinguished based on the chemical nature of the neighboring atoms. The compounds that were chosen for the study led to rate rules for P_1, P_2, P_3, S_{00}, S_{01}, S_{11}, T_{000} and T_{002} abstraction sites, where P, S and T refer to primary, secondary, and tertiary sites, and the subscript denotes the number of C atoms bonded to the NNN C atom of the C-H bond of interest [64]. For example, P_3 is a primary carbon bonded to a carbon connected to three other carbons (i.e., the neighbor is a quarternary site); and T_{002} is a tertiary carbon bonded to two primary carbons and one tertiary carbon. Badra et al. [65] conducted a similar study wherein they measured the total rate of H-atom abstraction by ȮH radicals from different molecules, including iso-octane. Based on their measurements, and the rate rules reported by [64], Badra et al. [65] derived rate rules for H-atom abstraction by ȮH radicals from S_{20}, S_{21}, S_{22}, S_{30}, S_{31}, S_{32}, S_{33}, T_{100} and T_{101} sites. The classification of abstraction sites in iso-octane based on NNN effects is shown in Fig.4.

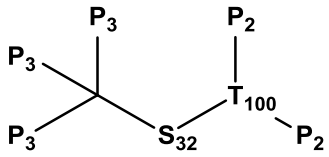

Figure 4. Carbon sites in iso-octane labeled according to the NNN methodology

Badra et al [65] proposed iso-octane rate coefficients for H-abstraction by ȮH radicals by adopting P_2 and P_3 rates from Sivaramakrishnan et al. [64] and S_{32} and T_{100} from their own work [65]. These [65] rate expressions yield a total abstraction rate constant profile that agrees with the experimental measurements for iso-octane [65]. The rates from [65] agree better than that which was previously employed in the iso-octane kinetic model by Mehl et al. [1], as demonstrated in Fig. 5. However, slight deviations between measurements and fittings were

observed at low temperatures, as shown in Fig. 5. Therefore, we re-calculated the rate coefficients of H-atom abstraction by ȮH radicals from S_{32} and T_{100} to better fit the experimental total rate constant profile reported by [65].

The re-calculated rate expressions are given below:

$$S_{32},\quad k(cm^3\ mol^{-1}\ s^{-1}) = 18.069\ T^{3.5}\ \exp\left(\frac{591.344}{T}\right)$$

$$T_{100},\ k(cm^3\ mol^{-1}\ s^{-1}) = 2.4092 \times 10^9\ T\ \exp\left(\frac{2.516}{T}\right)$$

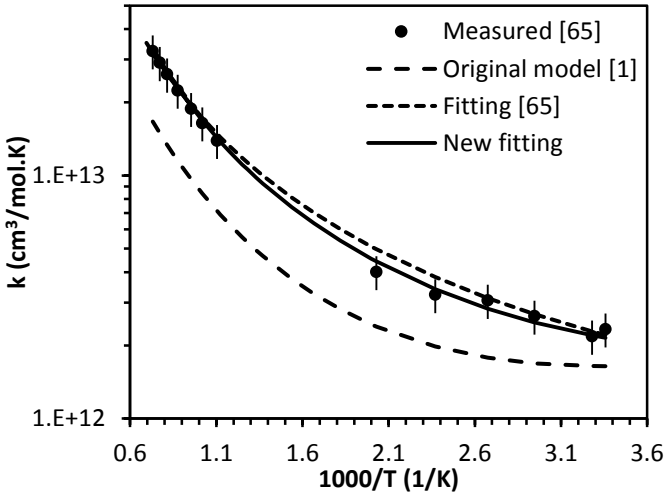

Figure 5. Experimental [65] and calculated total rate constant profiles for H-atom abstraction by ȮH radicals from iso-octane.

2-2-2 Addition of alkyl and hydroperoxy alkyl radicals to O_2

The rate rules proposed by Miyoshi [67] were used for the addition of iso-octyl radicals to O_2 to form alkylperoxy radicals (ROȮ). These rate rules are derived from energy calculations using variational transition state theory (VTST) and (RRKM)/master equation. The same rules were used for the addition of hydroperoxy-alkyl radicals (QOOH) to O_2 to form peroxy-alkylhydroperoxide radicals (ȮOQOOH); however, the rates were divided by 2, based on the findings of Goldsmith et al. [68]. Their calculations showed that the rate for second addition to O_2 (QOOH + O_2) is half that of the first addition to O_2 (R + O_2), and in accordance with other modeling studies [50, 51, 69].

2-2-3 Concerted elimination from ROȮ / ȮOQOOH to form olefin + $HȮ_2$

The third updated class is the concerted elimination to form olefins and $HȮ_2$ radicals from alkylperoxy radicals (ROȮ). This class of formally chain propagation reactions produces

relatively stable olefins and relatively less reactive $H\dot{O}_2$ radicals, effectively inhibiting reactivity and slowing ignition. Villano et al. [45] calculated the rate coefficients of these reactions for C_2 to C_6 alkylperoxy radicals using CBS-QB3 electronic structure calculations combined with B3LYP/6-31G(d,p) optimized geometries , and provided rate rules depending on the degree of substitution in the olefins produced. Based on their reported values, the formation of highly substituted olefins from alkylperoxy species is two to three times faster than that of less substituted olefins, which contributes to the lower reactivity of branched alkanes. The reaction kinetics involved in the potential energy surfaces of secondary and tertiary iso-octyl radicals + O_2, including concerted $H\dot{O}_2$ radical elimination reactions, were studied computationally by [42] and [43], respectively, both using optimized geometries from B3LYP/6-31G(d,p) and CBS-QB3 for the energy calculation. In both studies, it was shown that the calculated rate constants for different classes are in good agreement with those of analogous reactions available in the literature [45-48], except for the concerted elimination of $H\dot{O}_2$ radicals from the tertiary site.

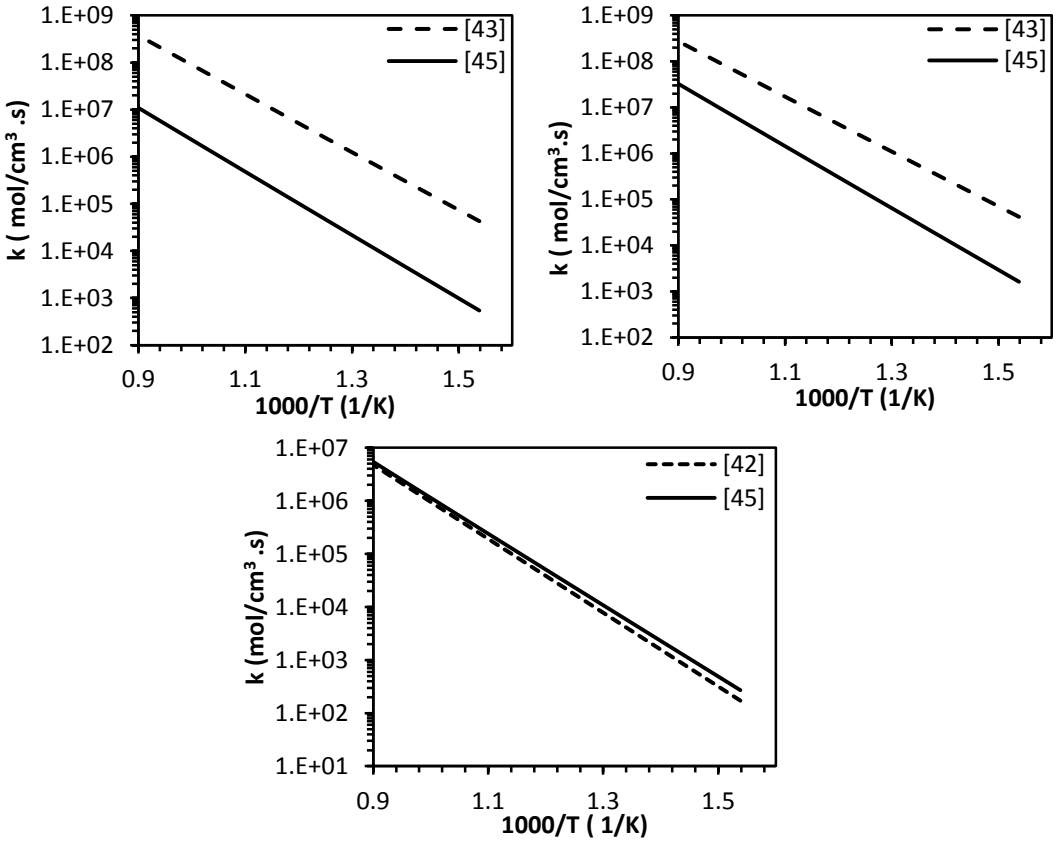

Figure 6. The rates of (upper left) $CC_8H_{17}\dot{O}_2$ <=> IC_8H_{16} + $H\dot{O}_2$ and (upper right) $CC_8H_{17}\dot{O}_2$<=>JC_8H_{16}+$H\dot{O}_2$ from Snitsiriwat et al. [43] vs Villano et al. [45]; and (bottom)

$BC_8H_{17}\dot{O}_2$<=>IC_8H_{16}+$H\dot{O}_2$ from Auzemendi-Murua et al. [42] vs Villano et al. [45]. See Supplementary material for species dictionary.

Figure 6 compares rate constants of concerted $H\dot{O}_2$ radical elimination for secondary and tertiary peroxy radicals calculated using Villano et al.'s [45] rate rules to those reported for iso-octyl peroxy by Auzmendi-Murua and Bozzelli [42] and Snitsiriwat and Bozzelli [43], respectively. As shown in Fig. 6, the rate constants obtained from [42] for the $H\dot{O}_2$ radical elimination from tertiary iso-octyl peroxy radicals are almost two orders of magnitude higher than those reported by [45] for tertiary peroxy, regardless of temperature. Therefore, for consistency, Villano et al.'s [45] rate rules of concerted HO_2-elimination were used for primary and secondary peroxy radicals, whereas Snitsiriwat and Bozzelli's [43] rate coefficients were used for the tertiary iso-octyl peroxy radical. By analogy, the rates calculated by Villano et al. [45] were also used for the concerted elimination from ȮOQOOH.

2-2-4 Isomerization of ROȮ and ȮOQOOH species and ketohydroperoxide (KHP) decomposition

Isomerization of ROȮ species involves the intra-molecular migration of a hydrogen atom from an alkyl group to the peroxy group via cyclic transition states, leading to the formation of hydroperoxy-alkyl radicals (QOOH). The rate coefficients of these reactions were taken from the computational study of Villano et al. [45], which provides rate rules depending on both the size of the transition state ring and the chemical nature of the alkyl group. The model includes isomerizations via 5,6,7 and 8 membered-ring transition states. The size of the transition and the nature of the migrating hydrogen atom (primary , secondary and tertiary) was considered when assigning the rates, as recommended by [45]. A comparison of isomerization rates for various transition state ring sizes and migrating hydrogen atoms is provided in Supplementary Fig.S3.

For ȮOQOOH isomerization, Sharma et al. [48] conducted a computational study at the CBS-QB3 and B3LYP/CBSB7 levels of theory with accurate treatment of hindered rotors. Their rate rules for isomerization of ȮOQOOH to ketohydroperoxides (KHP) were adopted in our study. However, since Sharma et al. [48] do not provide a rate rule for intra-molecular H-atom migration to a peroxy group at a tertiary site, the rate coefficients of this type of reaction were estimated based on the knowledge that the rate of abstraction gets progressively slower from tertiary to secondary and then primary carbons. The subsequent decomposition of KHP via O–O scission was assigned a rate constant with a frequency (A-) factor of 1.5×10^{16} s^{-1} and an

activation energy of 42.3 kcal mol^{-1} [69]. In addition, the H-exchange reactions in ȮOQOOH radicals from the hydroperoxy site to the peroxy (i.e., ȮOQOOH=HOOQOȮ) were added to the mechanism. The rate rules from Miyoshi [47] were adopted for this class.

2-2-5 Cyclic ether formation, and β-scission of QOOH species

Hydroperoxy-alkyl radicals (QOOH) undergo addition to molecular oxygen, cyclic ether formation, and *β*-scission reactions. The reactions involving QOOH radical addition to molecular oxygen have already been discussed above.

The *β*-scission reactions are divided into two classes; *β*-QOOH = olefin + $H\dot{O}_2$ and *β*-QOOH = olefin + carbonyl + OH. The formation of $H\dot{O}_2$ and olefin is favored due to the weakness of the C–OOH bond compared to a C–C or C–H bond. The rates of this reaction class were updated based on the computational rate rules published by Villano et al. [46]. They showed that the kinetics of this class is insensitive to carbon substitution(s) at the hydroperoxy or the radical site, and thus, they only provided one rate rule for this reaction class. The other class involving the formation of olefin, carbonyl and OH is less energetically favorable than the other pathways (addition to O_2 and cyclic ethers formation) due to the higher bond dissociation energy of C–C bonds compared to O–O and C–O bonds. This class was updated using the rate rules recommended by Bugler and co-workers [49] .

Another propagation reaction pathway for QOOH radicals is the formation of cyclic ethers + ȮH. The kinetics of such reactions were computationally studied by Villano et al. [46] and Miyoshi [47] at the CBS-QB3 level of theory. Villano et al. [46] found that the activation energies of these reactions vary depending on the thermochemistry of the specific reaction. Therefore, they reported rate rules with activation energies written as a function of standard heat of reaction (ΔH_{rxn}). Meanwhile, Miyoshi [47] distinguished between different cyclic ether formation reactions based on the degree of branching. As the number of substituents on the formed ring increases, the exothermicity of the reaction increases, implying that the rate of the reaction depends on the nature of the radical site and hydroperoxy site in the QOOH radical. In their work, Villano et al. [46] compared their calculated rate constants to those from Miyoshi's work [47] and both sets of rate rules gave good agreement.

However, when applied to iso-octane, the rate rules from [46] and [47] did not give similar rate constants for cyclic ether formation reactions. Figure 7 compares the rate constants of cyclic ether formation from $B\dot{C}_8H_{16}OOH$-A (7a), $C\dot{C}_8H_{16}OOH$-B (7b), $C\dot{C}_8H_{16}OOH$-D (7c) and $C\dot{C}_8H_{16}OOH$-A (7d) using the rate rules from Miyoshi [47] and Villano et al. [46] (see Supplementary material for species glossary).

When using Villano et al.'s [46] ΔH_{rxn}-dependent rate rules, three values of ΔH_{rxn} were tested in the comparison: i) computational values for ΔH_{rxn} from Bozzelli's group [42, 43] (solid black lines in Fig. 7), ii) THERM-calculated values with the corrections mentioned previously (dashed black line in Fig. 7), and iii) THERM-calculated values without the corrections (dotted black line in Fig. 7). Figure 7 clearly shows that the rate constants of cyclic ether formation reactions are highly sensitive to the thermochemistry of the reaction. The best agreement is observed between Miyoshi's [47] rate constants and those obtained using Villano et al.'s rate rules with ΔH_{rxn} calculated using computational values form Bozzelli's group [42, 43]. Since computational thermochemical properties are not available for all iso-octane QOOH and cyclic ether species, Miyoshi's rate rules for cyclic ether formation reactions were chosen in our model. The effect of using different sources for the rate constants of cyclic ether formation on iso-octane ignition delay profiles is shown in Fig. S2 of the Supplementary material.

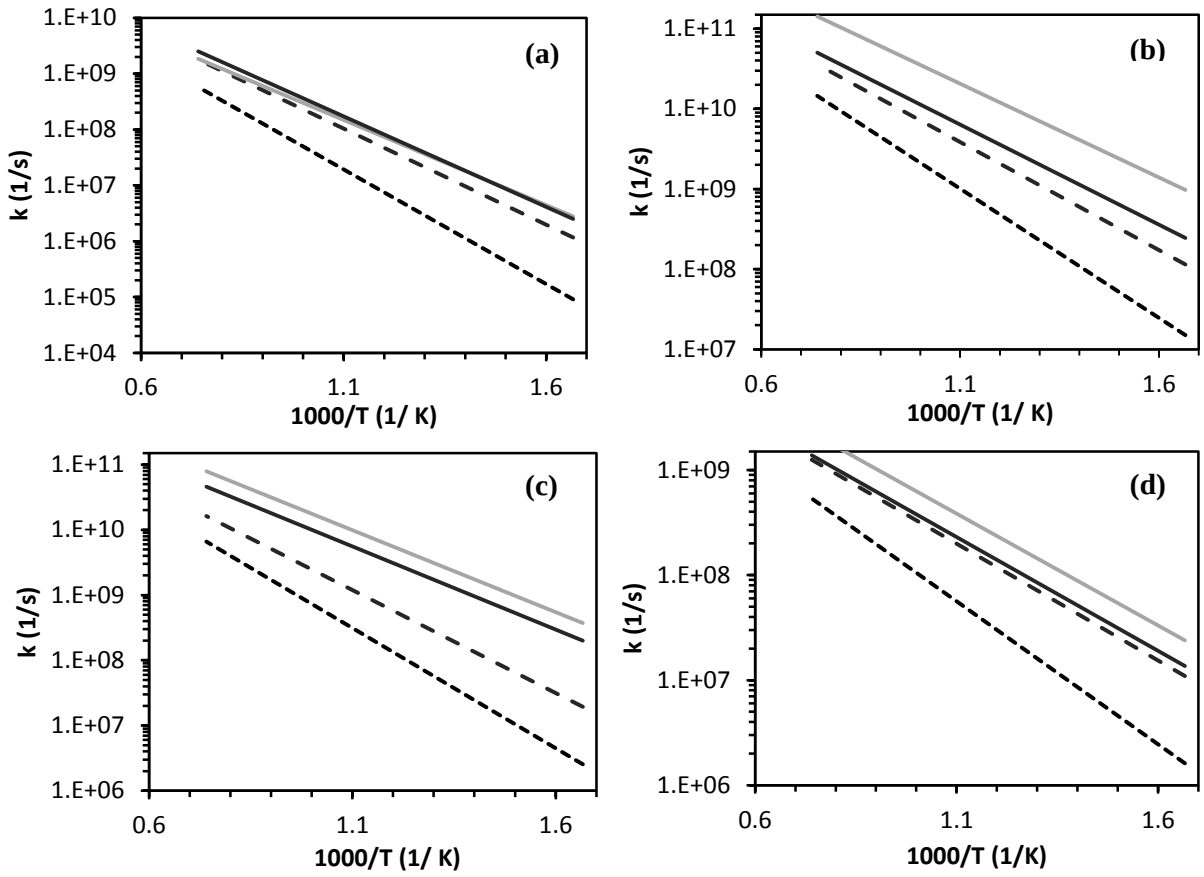

Figure 7. Rates of cyclic ether formation from (a) $B\dot{C}_8H_{16}OOH$-A, (b)$C\dot{C}_8H_{16}OOH$-B, (c) $C\dot{C}_8H_{16}OOH$-D, and (d) $C\dot{C}_8H_{16}OOH$-A calculated using Miyoshi's rate rules [47] (grey line), Villano's rate rules [46] with computationally calculated heats of formation from Bozzelli and co-workers [42,43] (solid black line), heat of formation from THERM after adding the corrections to the groups (dashed black line) and without adding these corrections (dotted black line).

2-3 Alternative isomerization pathways

In previously developed mechanisms [35, 36], the only reaction pathway available for peroxy-alkylhydroperoxide radicals (ȮOQOOH) was the formation of ketohydroperoxides (KHP) via intra-molecular H-atom migration from the C–H site connected to the peroxy group (i.e. COOH); this is followed by cleavage of the O–OH bond to form KHP and an ȮH radical. The H-atom at the COOH site is abstracted to form the ketohydroperoxide due to the weak C-H bond. However, recent studies [48-51, 69, 70] show that the intra-molecular migration of H-atoms from other carbon sites in ȮOQOOH radicals can be competitive. In their study on 2,5-dimethylhexane oxidation in a jet stirred reactor, Wang et al. [52] detected species with four and five oxygen

atoms that were not accounted for in conventional combustion mechanisms. Based on their findings, they proposed new oxidation pathways that are instigated by alternative isomerization of ȮOQOOH species to produce alkyl-dihydroperoxides ($P(OOH)_2$), followed by a third O_2 addition, or β-scission, or the formation of hydroperoxy cyclic ethers, as shown in Fig. 3. Later, Wang and Sarathy [53] showed the importance of the third O_2 addition pathway in simulating combustion in HCCI engines, and recommended the addition of this pathway to mechanisms of large alkanes (> C_6). Therefore, alternative isomerization and subsequent reactions of $P(OOH)_2$ species were added to our updated iso-octane model.

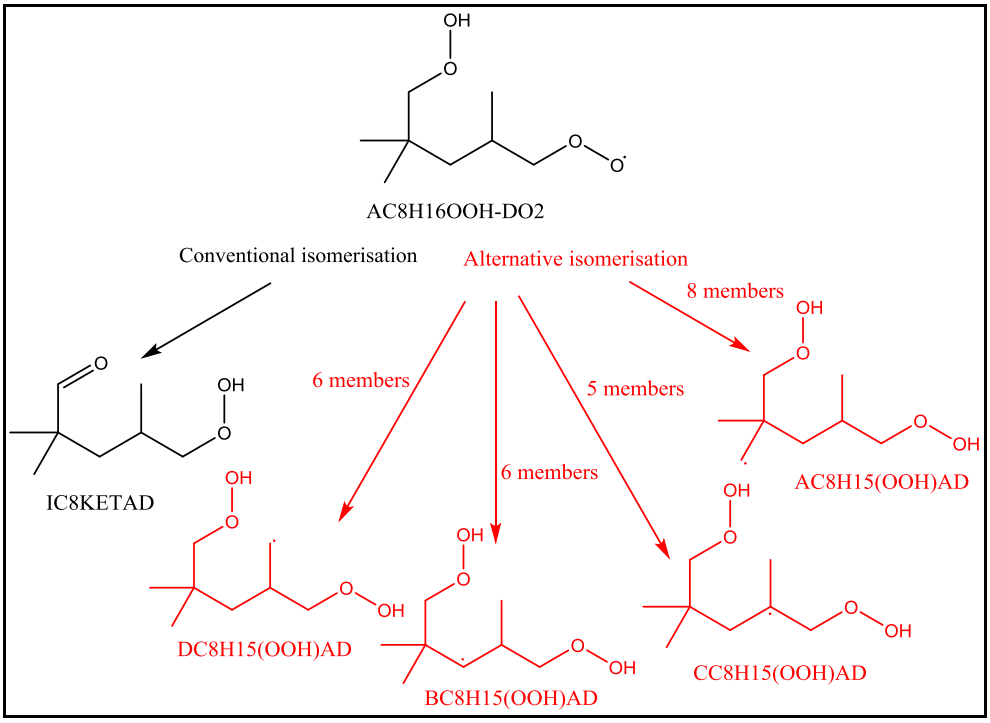

Figure 8. Conventional and alternative isomerization for one of the ȮOQOOH species

Since the added reactions have only been recently postulated, no information exists in the literature regarding their kinetics. Therefore, we used analogies and estimations to assign rate coefficients of these reactions. For alternative isomerization and β-scission of $P(OOH)_2$ species, we used Villano et al.'s [46] rate coefficients for RȮ/QOOH isomerization and β-scission of QOOH, respectively. Meanwhile, Miyoshi's [47] rate coefficients of cyclic ether formation were used for the formation of hydroperoxy cyclic ethers. Finally, Miyoshi's [47] coefficients for alkyl radical addition to O_2 were used for the third O_2 addition ($P(OOH)_2 + O_2$), with an A-factor divided by two, similar to the second addition to O_2 reactions.

The subsequent reaction pathway of $\dot{O}OP(OOH)_2$ species is isomerization to keto-dihydroperoxides (KDHP), for which Sharma et al.'s [48] KHP formation rate coefficients were used. Similar to KHP, the KDHP species decompose via O–OH bond scission. However, unlike the decomposition of KHP, for which the activation energy is 42.3 kcal mol^{-1}, the activation energy of KDHP decomposition was chosen as 39 kcal mol^{-1} following the recommendations of Sarathy et al. [63]. This value was assigned to better match experimental ignition delay profiles of iso-octane.

2-4 Performance of updated model

The addition of all of the aforementioned reaction pathways and rate constant updates led to a model that is too fast at low and intermediate temperatures, compared to experimental data [9], with an example comparison shown in Fig. 9.

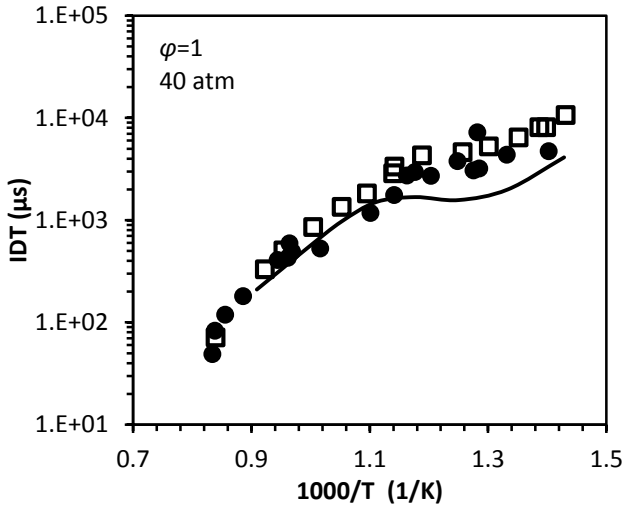

Figure 9. Simulated IDT using the updated and untuned model compared against experimental data from literature circles [9] and open squares [10] at 40 atm, stoichiometric iso-octane/air mixture

Further modifications to the rate rules, based on ȮH radical sensitivity analysis performed using CHEMKIN-PRO [71], were required to achieve better agreement between model-simulated and experimental ignition delay time profiles. Figure 10 shows that the QOOH radical plus O_2 reactions exhibit high and positive sensitivity coefficients, meaning that they promote the production of ȮH radicals and increase reactivity. Meanwhile, the competing pathways of cyclic ether formation from QOOH radicals have negative sensitivity coefficients and decrease

reactivity. The formation of cyclic ethers is a chain propagation pathway while the O_2 addition is a chain branching pathway, which illustrates their opposite effect on reactivity. The rate constants of these sensitive reactions were modified within their uncertainty limits, and model agreement with experimental data was tested after each modification. The best agreement was obtained when the rate constants of cyclic ether and hydroperoxide cyclic ether formation reactions for iso-octane moieties were doubled. The tuned reaction classes are shown in Table 2.

Table 2. Modifications to the rate parameters to fit the experimental data for iso-octane.

Rate	Reference	Modification
QOOH = cyclic ether + ȮH	[47]	A-factor × 2
$P(OOH)_2$ = hydroperoxy cyclic ether + ȮH	[47]	A-factor × 2
KDHP = ȮH + β-scission products	[63]	E_a=39 kcal

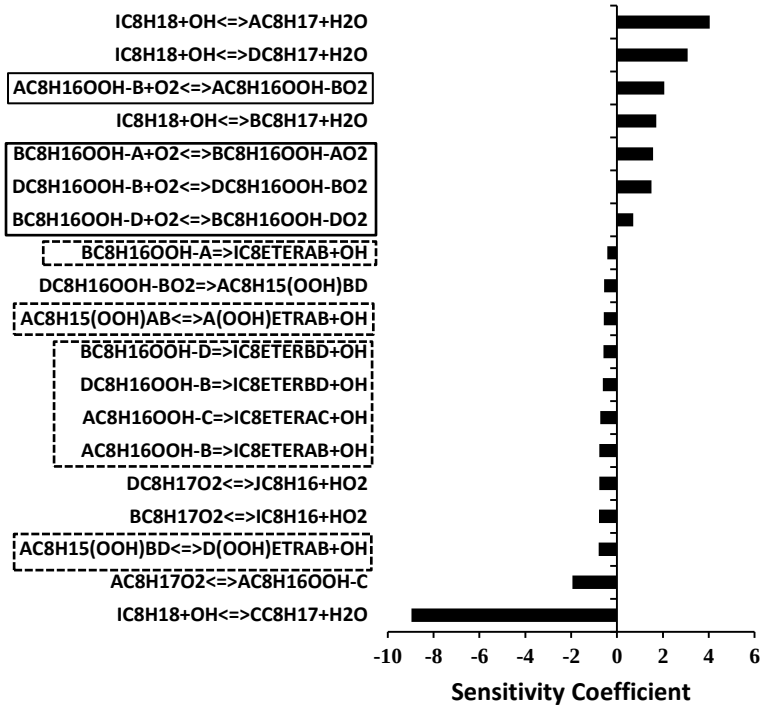

Figure 10. Sensitivity analysis to ȮH radicals at 750 K,40 atm, φ =1 at just before ignition. Rates of cyclic ethers formation and second O_2 addition are shown in dash-outlined and solid-outlined boxes, respectively.

3- Experimental

3-1 UCONN RCM

Experimental ignition delay time measurements at low and intermediate temperatures were conducted using rapid compression machines (RCM) at UCONN, NUIG and at KAUST. The UCONN RCM consists of a creviced piston that is driven pneumatically, and brought to rest hydraulically towards the end of compression. Compression occurs in a single stroke and the compression time is about 30–40 ms. The compression ratio can be varied by changing the stroke length and clearance volume independently. Pressure time history from the start of compression to post-ignition is measured using a Kistler 6125C pressure transducer along with a 5010B charge amplifier. Compressed pressures as high as 70 atm and pre-heated temperatures up to about 420 K can be attained in this RCM. Further details regarding this machine can be found in [72, 73]

Homogeneous fuel air mixtures were prepared in a stainless steel mixing chamber. Fuel was injected into the mixing chamber on a gravimetric measure using a syringe, whereas oxygen and diluent gases were filled in on a barometric measure. Ultra high purity (>99.99%) gases supplied from Airgas were used to prepare the mixtures, except for iso-octane, which was supplied by Sigma-Aldrich at high purity (>99.8%) by Sigma-Aldrich. A magnetic stirrer at the bottom of the mixing chamber was used to ensure homogeneity of the prepared gas mixtures. The fuel-oxidizer mixtures were allowed to mix in the chamber for about 2.5 hours.

The homogeneous fuel-air mixtures were compressed rapidly to the desired pressure and temperature. The compressed temperature was estimated using the adiabatic-core hypothesis. Subsequent to compression and after an induction period, a rapid rise in pressure was observed due to auto-ignition. Ignition delay time is defined as the time interval between the end of compression and the maximum rate of pressure rise. First- (τ_1) and total ignition delays (τ) are defined similarly. This definition of ignition delay is illustrated in Fig. S4. A minimum of 5 concordant experimental runs were carried out for each data point reported. A representative experimental pressure trace close to the mean is chosen for reporting the ignition delay. The typical scatter in ignition delay time is ~10% of the reported value and the temperature uncertainty is ±5 K. Figure S5 demonstrates the typical repeatability. Inert runs wherein oxygen

was replaced by nitrogen were conducted at every set of temperature, pressure and equivalence ratio condition in order to infer the heat loss characteristics during the compression stroke and the post-compression period.

Experiments were conducted in the low-to-intermediate temperature range with temperature at end of compression (T_C) varying between 640 K and 960 K at equivalence ratios of 0.4 and 1 in air. High compressed pressures of nominal p_C near 20 and 40 atm are investigated herein.

3-2 KAUST RCM

The rapid compression machine (RCM) facility at KAUST is based on a twin-opposed piston design similar to the one used at NUIG [74]. The combustion chamber bore is 5.08 cm and, based on the final piston spacing, the volumetric compression ratio can be adjusted up to 16.8. The characteristic time required for the final 50% of the pressure rise during the compression phase is about 3 ms. The piston heads are creviced to minimize boundary layer mixing with the core gas. The gas mixtures are prepared in a 20 L stainless steel magnetically stirred mixing vessel. The temperature of the vessel and the combustion chamber can be increased using heating jackets. The compressed gas temperature at the end-of-compression (EOC) is computed by applying the following isentropic relation on the measured pressure trace:

$$\int_{T_I}^{T_C} \frac{\gamma}{\gamma - 1} \frac{\mathrm{d}T}{T} = \ln\left(\frac{p_C}{p_I}\right)$$

where, the subscripts *C* and *I* refer to the EOC (end of compression) and initial conditions, respectively. The diluent was varied from pure nitrogen to a mixture of nitrogen and argon to reach temperatures up to 950 K and a mixture of nitrogen and carbon dioxide to reach temperatures down to 635 K. Six axisymmetric ports are present on the central axial location of the combustion chamber for optical access, gas exchange and the pressure transducer (Kistler 6045A). The ignition delay time for this work was determined from the maximum pressure rise in the measured pressure trace. The uncertainty in the ignition delay measurement was approximately +/- 10%.

3-3 NUIG RCM

Low- to intermediate-temperature (650-1000 K) ignition delay times for stoichiometric mixtures of iso-octane in a 21:79 oxygen to diluent bath gas at nominal pressures of 15 near 15 and 20 atm were measured in two RCM facilities at NUIG; low compression piston head (LCPH) and high compression piston head (HCPH). The details of the experimental platform and the methodology used to measure fuel ignition delay times within the device have been extensively documented in [51, 75-78] therefore only a brief description of the apparatus is given here.

Briefly, the device volumetrically compresses a test gas to a high temperature and pressure condition, and allows an isochoric reaction to proceed after compression within the high-energy gas. The compressed gas pressure is varied by adjusting the initial gas pressure in the reaction chamber, while the compressed gas temperature is varied by altering the initial temperature of the reaction chamber as well as by tailoring the composition (specific heat) of the non-reactive diluent gases. The transient pressure history of the test gas is monitored during the experiment by a Kistler 6045A pressure transducer that is mounted in the sidewall of the reaction chamber. Ignition delay times are measured from the test gas pressure history, and defined as the time difference between the local maximum in pressure that occurs near the end of volumetric compression and the maximum rate of pressure rise due to ignition. The widely used adiabatic core model [72, 79] is employed to evaluate the compressed gas temperatures from pressure histories. Furthermore, the adiabatic core model is also used to transiently prescribe the energy supplied to or lost from the test gases due to volumetric compression and heat losses, respectively, in order to adequately compare experimental data sets with mechanism simulations. These transport processes are isolated from chemical ones by compressing an analogous non-reactive gas for each experimental condition (where the reactive gas oxygen fraction is substituted by nitrogen), and quantified by deriving the specific volume history of the adiabatic core gas from the measured pressure history of the non-reactive experiment that is then used as an input boundary condition for a simulated variable volume 0-D reactor. The uncertainty in the ignition delay measurement is approximately +/- 15%.

The fuel burned in this study was provided by Sigma-Aldrich (99.8% pure), while nitrogen (99.95%), oxygen (99.5%) and argon (99.5%) gases were supplied by BOC Ireland.

3-4 KAUST HPST

The high-pressure shock tube (HPST) facility has been previously described in detail in [80], so only a brief overview is given here. The facility consists of a stainless steel, electropolished tube divided by aluminum diaphragms into a 6.6 m driven section and a modular driver section that can be extended up to 6.6 m. The inner diameter of the tube is 10 cm. The measurements were conducted at the reflected shock conditions via a pressure transducer (Kistler 6045A) mounted at a distance of 1 cm from the shock tube endwall. The reflected shock conditions are determined from the incident shock wave velocity measurements using five axially spaced pressure transducers (PCB113B26) over the last 3.2 m length of the driven section. The reactant mixture was prepared in a 40 L stainless steel mixing vessel equipped with a magnetic stirrer. The vessel and shock tube were heated to 80 ^{0}C for these experiments using heating jackets to prevent fuel condensation. As with the RCM, the ignition delay time is determined by the time of maximum pressure rise. The uncertainty in the ignition delay measurement is +/-20 %. A non-ideal pressure rise (*dp/dt*) of approximately +3% /ms was observed behind the reflected shock wave in these experiments. This non-ideality is accounted for in numerical shock tube simulations using a representative volume profile. Example pressure traces for shock tube ignition delay measurements are illustrated in Fig. S6 of the Supplementary material. Several pressure traces at lower temperatures (i.e., longer ignition delay times) exhibited significant pre-ignition pressure rise that may be caused by inhomogeneous ignition [81, 82].

4- Results and Discussion

4-1 Model validation against new experimental data

The chemical kinetic model was compared against experimental data at a range of conditions, including newly acquired data and data available in the literature, as shown in Table 3. The experimentally measured ignition delay time profiles were simulated using the closed homogeneous batch reactor model in CHEMKIN-PRO software [71] along with the updated iso-octane model. In order to account for heat losses, RCM experiments were simulated using experimentally determined variable volume profiles. These volume profiles are available as supplementary material.

Table 3. Summary of experimental conditions employed for validating iso-octane model.

Technique	Pressure (atm)	Equivalence Ratio φ	Temperature range (K)	% Fuel	Diluent	Reference
ST ignition	50	0.5,1	700-1200	100%	air	[9, 10]
ST ignition	10-50	0.25,0.5, 1	870-1250	100%	air	[8]
ST ignition	14,17,50	0.5, 1	855-1170	100%	air	[7]
ST ignition	1.4	0.5,1,2	1250-1810	0.25%,0.5%,1%	Ar	[6]
ST ignition	20	1	893-1060	100%	air	KAUST*
JSR oxidation	10	0.3,0.5,1,1.5	750-1100	0.1%	N_2	[32]
Laminar flame speed	1	0.6-1.7	298,355	100%	air	[21, 24-26, 28, 29]
Laminar flame speed	10	0.8-1.1	323,373,423,473	100%	air	[23]
RCM ignition	15,20	1	635-787	100%	100% N_2	NUIG*
			765-965	100%	25%N_2/75%Ar	
RCM ignition	20,40	0.4,1	632-958	100%	100% N_2	UCONN*
RCM ignition	20	1	632,655	100%	80%CO_2/20%N_2	KAUST*
			666-813	100%	100% N_2	
			851-948	100%	20%N_2/80%Ar	
ST pyrolysis	25,50		900-1700	137, 149 ppm	Ar	[12]

*This study

Figure 11 shows a comparison of the simulated ignition delay time (IDT) profiles to those measured experimentally using the RCM facility at UCONN. Simulations were conducted using the updated iso-octane model developed in this study, as well as the original model developed by Mehl et al. [1]. As shown in Fig. 11, the updated model matches the experimental data better than the original one, particularly at $\varphi = 0.4$. Matching the reactivity under fuel-lean conditions is crucial for HCCI engine simulations because those engines are typically operated at equivalence

ratios of less than 0.5. The updated model under predicts the measured ignition delay times by nearly a factor of two at the lowest temperature conditions at φ = 0.4, 40 bar and φ = 1, 20 and 40 bar. At φ = 0.4, 20 bar, the model slightly over predicts the measured ignition delay time. Despite the improved agreement between the updated model and experimental data at φ = 0.4 and p_C = 20 atm, the updated model shows higher reactivity at φ = 1 and p_C = 20 atm for temperatures higher than 750 K. This discrepancy warranted further investigation.

In order to ensure the validity of RCM experiments conducted at UCONN, particularly at conditions where significant discrepancies were observed between experimental and simulated data, the same experiments (φ = 1 and p_C = 20 atm) were run using RCM facilities at NUIG and at KAUST. However, as mentioned earlier, experiments at UCONN were conducted in air (O_2/N_2), whereas Argon was added to Nitrogen bath gas at NUIG and at KAUST to achieve high temperatures at EOC (end of compression). Figure 12a shows that for temperatures greater than 850 K, NUIG and KAUST RCM ignition delay data do not match those recorded at UCONN. This discrepancy is a attributed to the diluent effect, which was thoroughly discussed by Würmel et al. [77]; they argued that substituting nitrogen by argon increases the ignition delay time in RCM experiments due to the cooling effect of argon in the post compression period. As shown in Fig. 12, for temperatures greater than 850 K the ignition delay times measured by NUIG (diluent gas is 25% N_2 and 75% Ar) and KAUST (diluent gas is 20% N_2 and 80% Ar) are longer than those measured by UCONN (diluent gas is only N_2). The diluent effect is not observed at 630 K and 655 K where 80% CO_2/20% N_2 were used as diluent at KAUST compared to 100% N_2 at NUIG and UCONN. This is largely due to the lower heat loss due to the lower thermal diffusivities (with correspondingly lower thermal conductivities and higher heat capacities) of N_2 and CO_2.

The diluent effect was not observed in simulated ignition delay times when comparing those under NUIG and UCONN conditions, as shown in Fig. 12a. For example, simulated ignition delay times using the inert volume profiles and bath gas conditions from UCONN and NUIG show similar ignition delay times at all temperatures. Simulations at the KAUST conditions (i.e., volume profiles and inert composition) show longer ignition delay times compared to the UCONN simulations due to the use of Ar as the diluent, but the differences are not as prominent as those observed experimentally. A comparison of the inert pressure and temperature traces at

850 K from UCONN (O_2/N_2) , NUIG (O_2/ N_2/Ar) and KAUST (O_2/ N_2/Ar) is shown in Fig. S7 in the Supplementary Material. It is interesting to note that the pressure and temperature profiles after TDC are similar for both facilities, which indicates similar heat-loss characteristics.

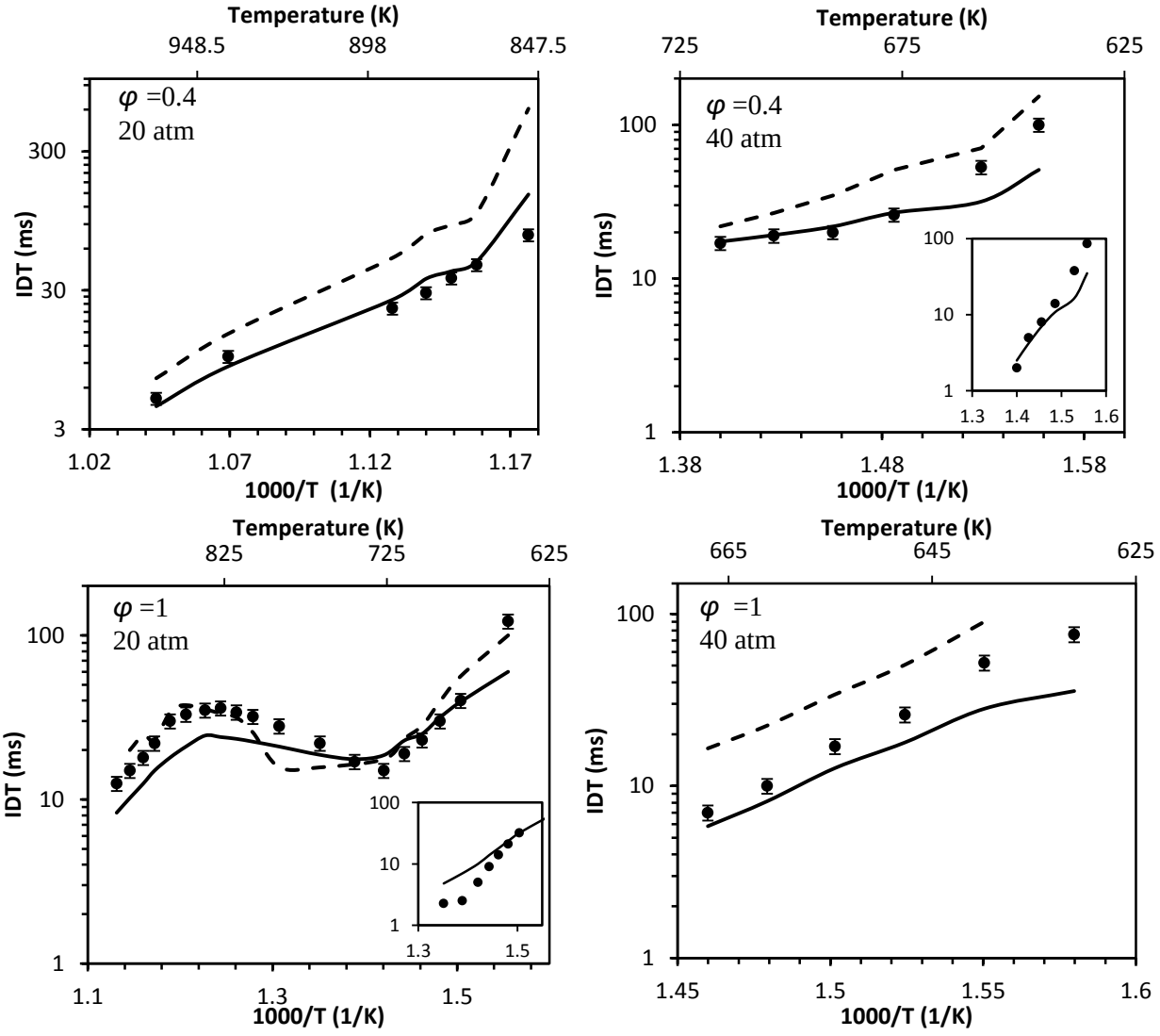

Figure 11. Iso-octane/air ignition delay times measured at the UCONN RCM facility and the corresponding simulations. Left panels are 20 atm while right panel are 40 atm. Upper panels are 0.4 equivalence ratio and lower panels are stoichiometric. Solid and dashed lines represent simulations using the updated model and original model [1], respectively. The insets show first stage IDT profiles.

Wagnon and Wooldridge [83] studied the effect of buffer gas composition on autoignition of stoichiometric mixtures of three different fuels; iso-octane, *n*-heptane and *n*-butanol. Their results emphasized the effect of the bath gas composition on low temperature combustion

chemistry through $H\dot{O}_2$ radical and H_2O_2 recombination and decomposition reactions, which are pressure dependent. They showed that different bath gases have different collision efficiencies, which affects the second stage ignition delay time. They compared experimental data for n-heptane ignition using different diluents (Ar and N_2) and showed that ignition is faster in the presence of Ar at high temperatures (>750 K); however their simulations were not able to capture the same difference.

Figure 12a shows a typical trend for the reactivity of alkanes. At low temperature, reactivity increases with increasing temperature and then starts to be inversely proportional to temperature. This region is known as the negative temperature coefficient regime (NTC), which is characterized by the competition between chain branching reactions, mainly isomerization of $\dot{O}OQOOH$ compounds (production of keto hydroperoxides), and chain propagation reactions, such as the formation of cyclic ethers and olefins from QOOH species (QOOH = cyclic ether + $\dot{O}H$ and QOOH = olefin + $H\dot{O}_2$). After the NTC region, reactivity is more controlled by high-temperature chemistry and $H\dot{O}_2$ radical chemistry, and again increases with increasing temperature.

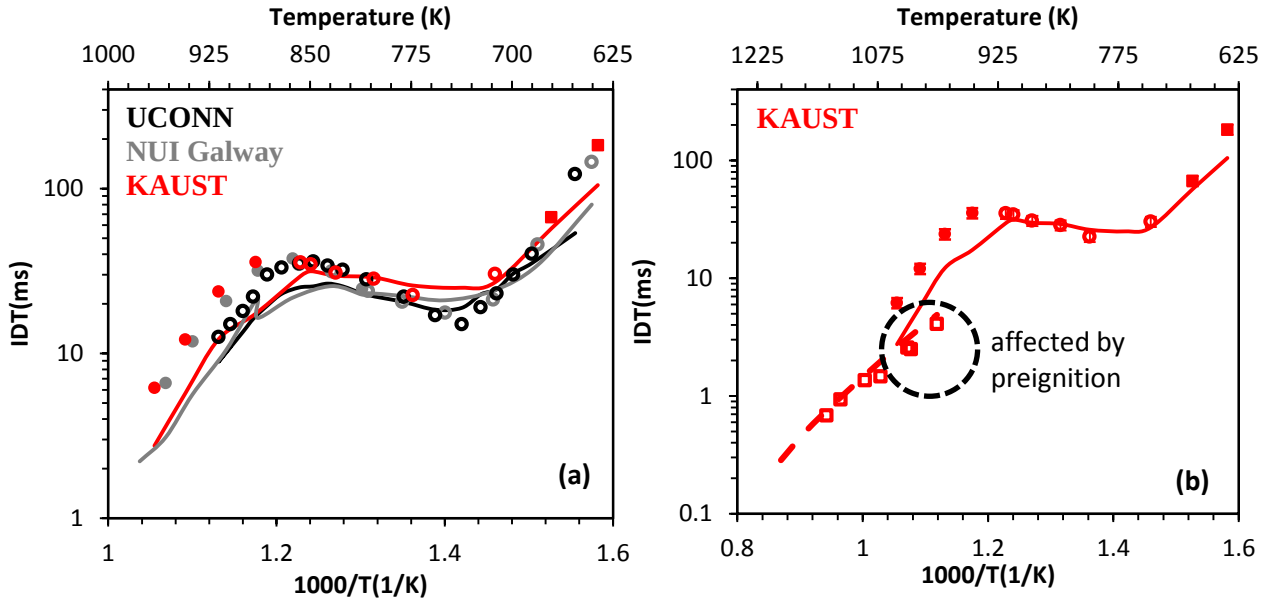

Figure 12. Iso-octane/oxygen/diluent ignition delay times at φ = 1 and 20 atm from (a) various RCM facilities and (b) KAUST ST and RCM. Solid lines are variable volume simulations while dashed lines are constant volume simulations in (b). Open and closed circles represent RCM experiments with only N_2 and N_2+Ar bath gases, respectively. Closed squares represent RCM

experiments with N_2+CO_2 diluent while open squares in (b) represent KAUST shock tube experiments. Dashed circle identified shock tube experiments that exhibited significant pre-ignition heat release. See digital paper for color version of this figure

To further understand discrepancies between simulated and experimental measurements, ignition delay times measured in the KAUST HPST are presented in Fig. 12b and compared with the KAUST RCM data and simulations. The HPST simulations include 3% per millisecond (*dp/dt*) pressure rise rate. An interesting observation in Fig. 12b is a factor of 3 discrepancy in IDT between the HPST and RCM experiments at an intermediate temperature T_C of ~ 870 K. This phenomenon was noticed in previous studies [38, 84, 85] of other high-octane fuels, but the reason for this difference is not yet identified. It may be attributed to the invalidity of the homogeneous core assumption of the RCM due to mass loss in the facility crevices or heat loss through walls. Inhomogeneity and boundary layer phenomenon in the shock tube may also contribute to the discrepancy. The updated kinetic model captures the IDTs measured by the HPST at temperature above 900 K, but the model is more reactive when compared to the RCM data these temperatures. It is worth restating that HPST experiments at low temperatures (933 K, 928 K and 894 K see dashed circle in Fig. 12b) exhibited non-ideal pre-ignition pressure rise, as shown in Fig. S5 in the Supplementary material. These conditions exhibited significant pre-ignition pressure rise (above 3%/ms) due to inhomogeneous ignition phenomenon [81, 82]. Various shock tube groups, including KAUST, are exploring such inhomogeneous ignition phenomena in detail to understand their causes, their effect on ignition measurements and potential remedies. Such discussions and illustrations are beyond the scope of the current work. It should be noted that experimental measurements exhibiting pre-ignition pressure rise cannot be accurately modeled using 0-D simulations, and therefore are not suitable targets for kinetic model validation/optimization.

The performance of the updated model is also compared to a recently optimized model by Cai and Pitsch [86] in which the rate rules assigned by Curran et al. [35] were calibrated to match the ignition delay time for iso-octane in [10], which limits the agreement of the model to a broader set of target data. The simulation results from both models compared to the new RCM experiments from UCONN are shown in Fig. S8 in the Supplementary material. The present model reproduces the RCM experimental data better than the optimized model of Cai and Pitsch

[86]. The optimized model [86] could be improved by including the new data as targets for the model optimization.

Figure 13 shows the ignition delay time for stoichiometric iso-octane mixtures using different diluents at 15 atm and 20 atm in the NUIG RCM. Decreasing the pressure decreases the reactivity due to lower rate of production of ȮH radicals from H_2O_2 (+M) = ȮH + ȮH (+M), a pressure dependent reaction. In addition, high pressure promotes low temperature chemistry, specifically alky radicals addition to O_2. Overall, the model shows good agreement with the experimental data at low and intermediate temperatures; however, the model is more reactive than the experiments at higher temperatures.

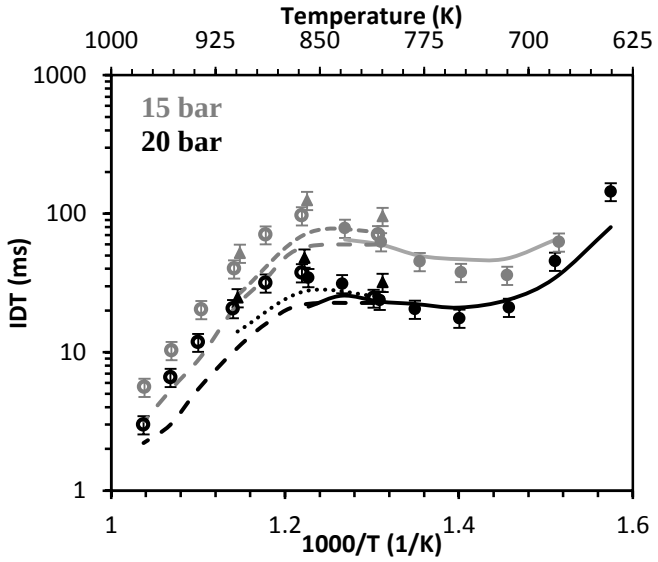

Figure 13. Iso-octane/air ignition delay times at φ =1 and 15 atm and 20 atm. Closed circles and straight lines represent experiments and simulations respectively with only N_2 as diluent in LCPH RCM. Triangles and dotted lines represent experiments and simulations in HCPH RCM with only N_2 as diluent. Open circles and dashed lines represent experiments and simulations with 20% N_2 and & 80% Ar diluent.

4-2 Model validation against experimental data in literature

4-2-1 Shock tube ignition delay data

The updated chemical kinetic model was used to simulate shock tube experiments from the literature. The simulations were carried out using the constant volume batch reactor code in

CHEMKIN-PRO [71] assuming homogeneous and adiabatic conditions behind the reflected shock wave.

Hartmann et al. [9] and Fieweger et al. [10] measured ignition delay times of iso-octane/air mixtures at 40 atm and φ = 0.5 and 1.0 in a high pressure shock tube. Figure 14 shows the experimental and simulated ignition delay time profiles over the temperature range 700–1200 K. The reactivity at this temperature range is sensitive to the equivalence ratio of the mixture because chain branching is dominated by KHP production. The leaner the mixture, the lower the fuel concentration and the less KHP produced, which results in a less reactive system [36]. Figure 14 also shows that the present model offers improved agreement with experimental data when compared with the original model by Mehl et al. [1].

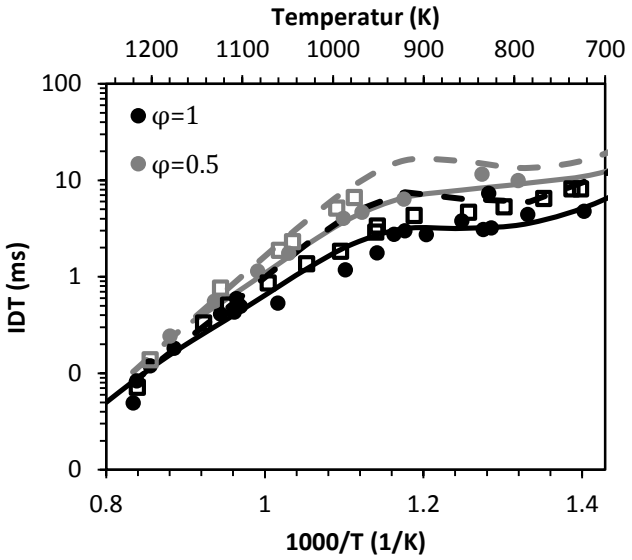

Figure 14. Iso-octane/air ignition delay times at 40 atm and equivalence ratios of 0.5 and 1.0. Experiments are from [9] (circles) and [10] (open squares). Simulations (lines) with the updated and original model [1] are represented by solid and dashed lines, respectively.

Shen and co-workers [8] carried out ignition delay time experiments of iso-octane/air mixtures in a high-pressure shock tube at different equivalence ratios (0.25, 0.5 and 1.0) and at pressures of 10, 12, 25, 45 and 50 atm. Their experimental data, and those simulated by our updated model and the original model [1] at the same conditions, are presented in Fig. 15. Both models match the experimental data relatively well at all investigated conditions, with better predictions for the updated model at high pressures and low temperatures.

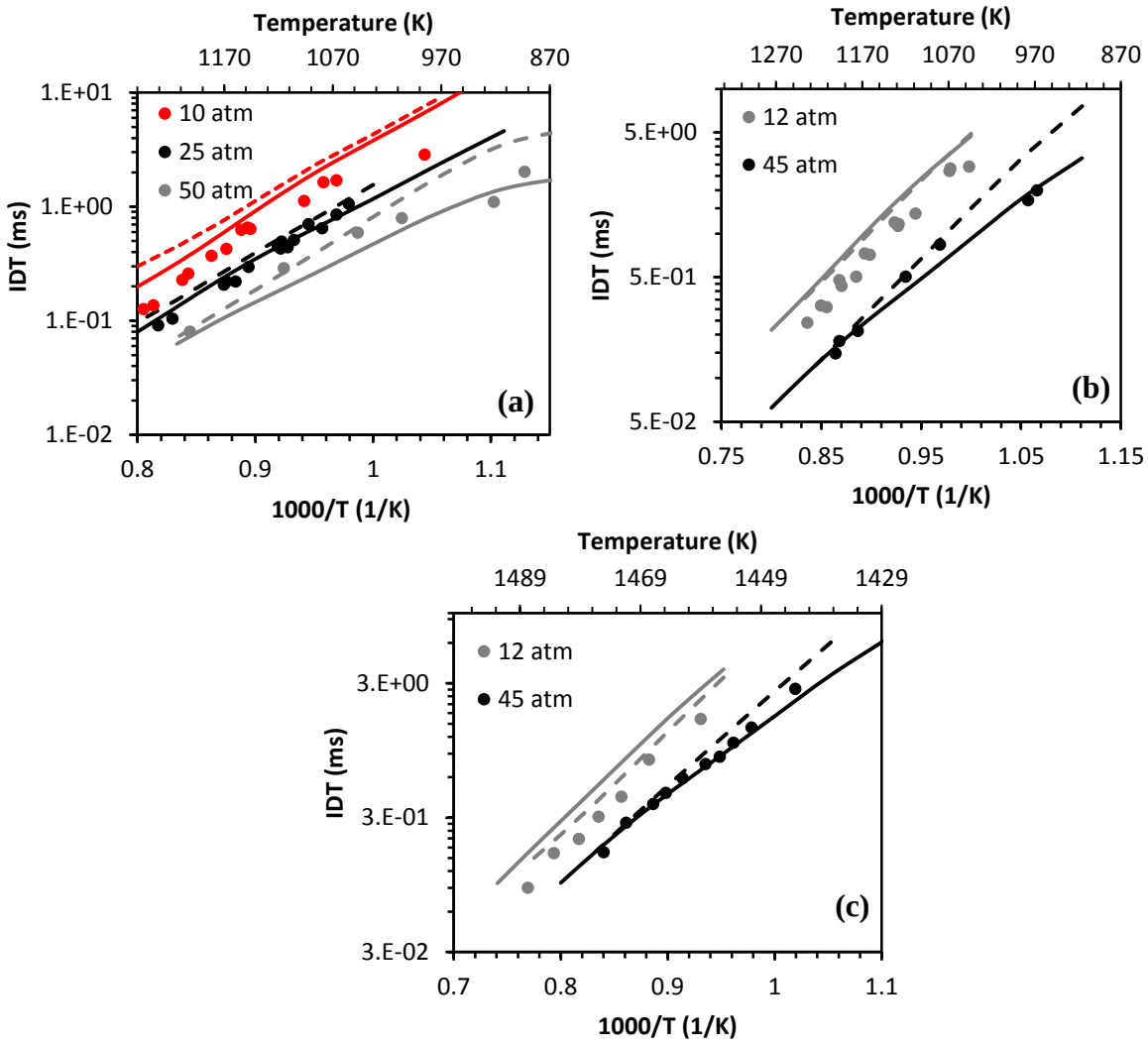

Figure 15. Iso-octane/air ignition delay times at various pressures and (a) φ = 1.0, (b) φ = 0.5, and (c) φ = 0.25. Experiments are from [8] (symbols). Simulations (lines) with the updated and original [1] model are represented by solid and dashed lines, respectively. See digital paper for color version of this figure.

Shock tube iso-octane oxidation experiments were also conducted by Davidson and coworkers [7] for fuel/air mixtures at pressures between 14 atm and 59 atm, temperatures between 855 K and 1270 K, and equivalence ratios of 0.5 and 1. Figure 16 compares the experimental IDT profiles from [7] to those simulated using the updated and original [1] iso-octane models. The updated model is more reactive than the original one at high pressures and low temperatures, which gives better agreement with experimental data at these conditions, particularly at φ =1.0.

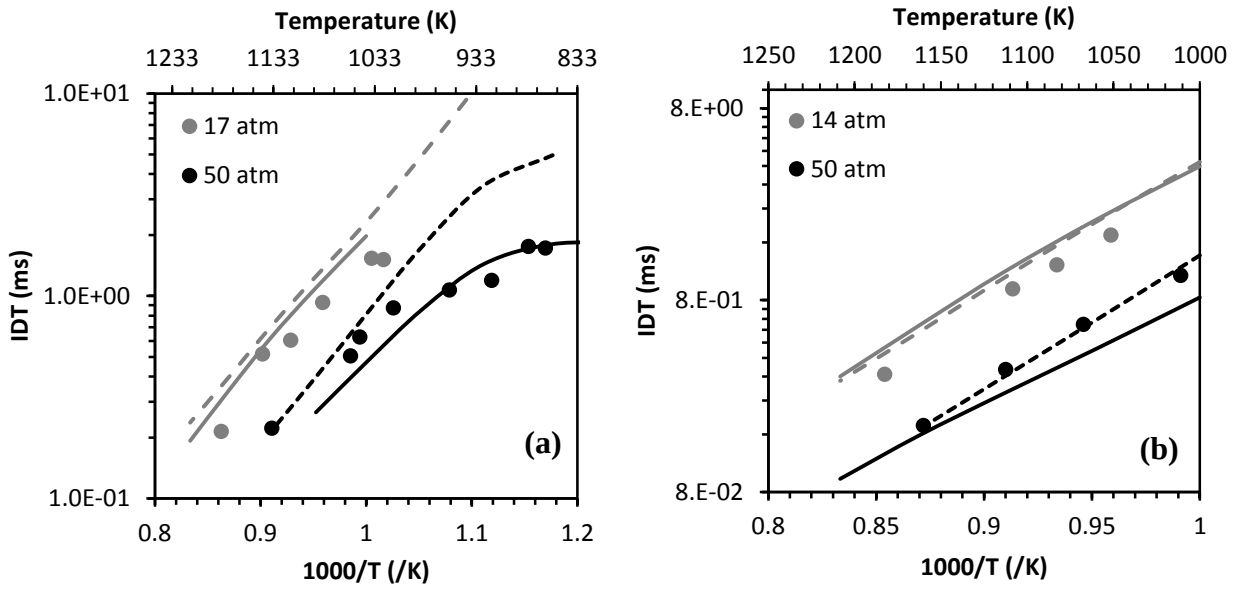

Figure 16. Iso-octane/air ignition delay times at two pressure and (a) φ = 1.0 and (b) φ =0.5. Experiments are from [7] (symbols). Simulations (lines) with the updated and original model [1] are represented by solid and dashed lines, respectively.

Oehlschlaeger et al. [6] used a shock tube to measure IDT for iso-octane/O_2/Ar mixtures at 1.4 atm and 0.5 < φ < 2 using different fuel concentrations (0.25%, 0.5% and 1%). Figure 17 compares experimental data from [6] to those simulated using the updated and original models. Both models show good agreement with the experimental data. However, for 1% fuel in air mixtures, the updated model is more reactive than the original one, especially at lower temperatures, and shows better agreement with experimental data.

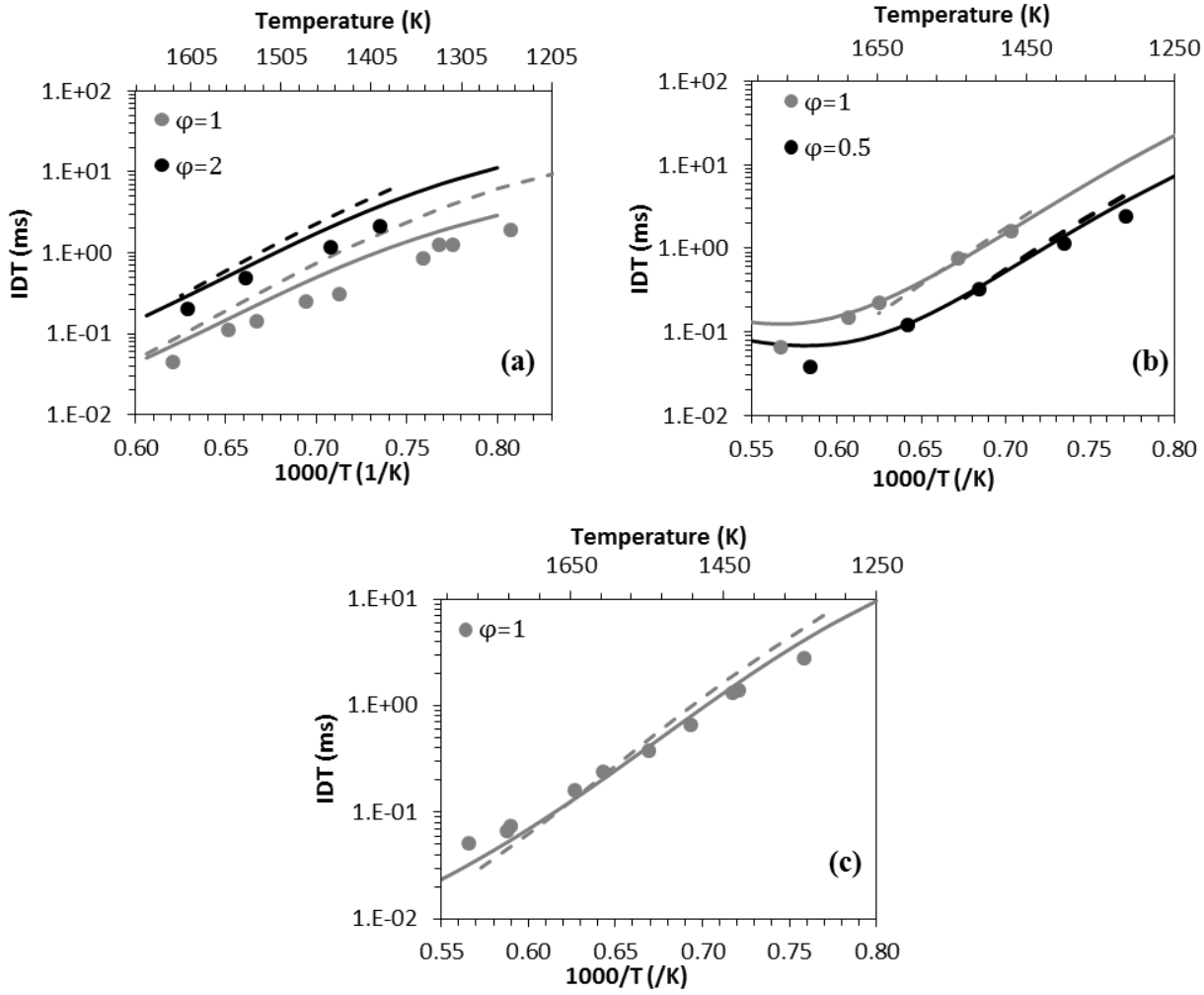

Figure 17. Iso-octane/O_2/Ar ignition delay times at 1.4 atm, various equivalence ratios, and fuel concentrations of (a) 1%, (b) 0.25%, and (c) 0. 5%. Experiment are from [6] (symbols). Simulations with updated and original [1] models are represented by solid and dashed lines, respectively.

4-2-2 Jet Stirred Reactor data

Dagaut et al. [32] carried out iso-octane oxidation experiments in a JSR for 0.1% fuel/oxidizer mixtures at φ = 0.3, 0.5, 1.0 and 1.5. The experiments were performed at 10 atm and with a mean residence time of 1 s. Gas chromatography and mass spectrometry were used to identify and quantify intermediates formed during iso-octane oxidation. The updated iso-octane model was compared against species concentration profiles measured in [32] using the perfectly stirred reactor code in CHEMKIN-PRO [71] with a transient solver to obtain a steady-state solution.

Figures [18-21] show the experimental and simulation profiles for different species at the four experimentally investigated equivalence ratios. Qualitatively, the updated model matches the experimental concentration profiles of all species detected species which include iso-octane, CO, CO_2, O_2, CH_4, H_2, CH_2O, C_2H_4, C_3H_6, iso-butene, 2,4-dimethyl-1-pentene, 2,4-dimethyl-2-pentene and 4,4-dimethyl-1-pentene. The profiles of iso-octane, carbon monoxide (CO), and carbon dioxide (CO_2) are well captured by the model at different equivalence ratios. Based on the shape of the iso-octane and CO profiles, neither the simulations nor experiments showed NTC behavior at the conditions studied. At all investigated conditions, CO concentrations are lower than those of CO_2; however, the concentration profiles of these species cross over at lean conditions as a result of oxidation of CO to form CO_2 at high temperatures. The leaner the mixture, the lower is the crossover temperature. In the presented data, the crossover temperature is 1000 K and 1050 K for φ = 0.3 and 0.5, respectively. The simulated concentration profiles of H_2, CH_4 and CH_2O agree well with those measured experimentally at φ = 0.5, 1.0 and 1.5. For φ = 0.3, H_2 concentrations are under predicted by 51% whereas CH_2O concentrations are over predicted by 36% at peak values. CH_4 concentrations are under-predicted below 900 K and over-predicted above 900 K.

The concentration profiles of C_2H_4 and C_3H_6 are quantitatively well predicted by the model at fuel-rich and stoichiometric conditions; however, the peak concentrations are under-predicted by 50–61% and 41–44%, respectively, at fuel-lean conditions. The predicted profiles as a function are temperature for 2,4-dimethyl-1-pentene (XC_7H_{14}), 2,4-dimethyl-2-pentene (YC_7H_{14}) and 4,4-dimethyl-1-pentene (PC_7H_{14}), the β-scission products of iso-octyl radicals, are generally broader that the experimental measurements. However, the maximum concentrations of YC_7H_{14} and PC_7H_{14} are under predicted with maximum deviation at φ = 0.3 of 52% and 73%, respectively.

Also Figs. S9-S12 in the Suppllementary material show the simulated species profiles using the Mehl et al. [1] model. Generally, the updated model shows a better agreement for all species.

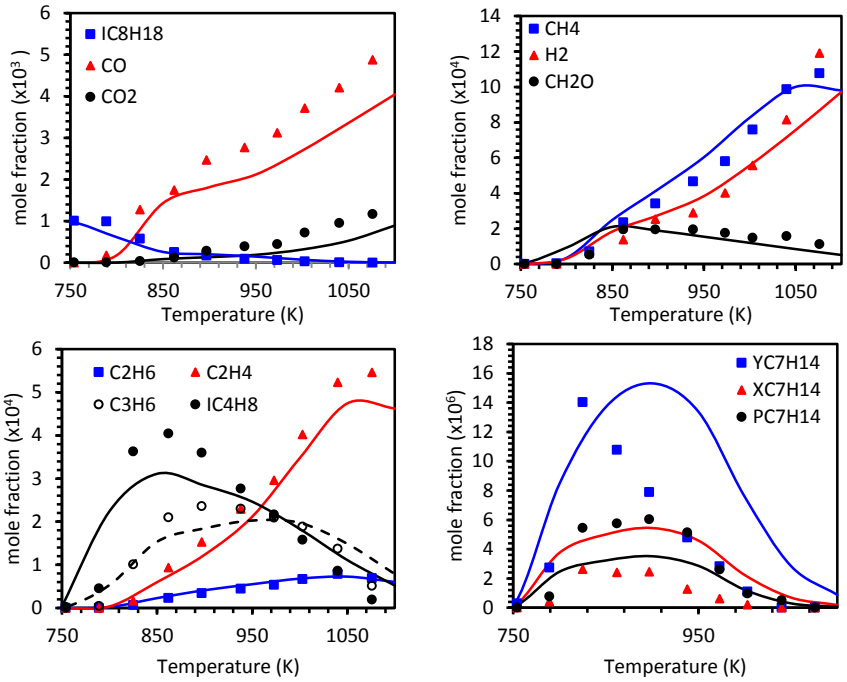

Figure 18. JSR species concentration profiles (points) and simulations (lines) using updated model (straight lines) and original model [1] (dashed lines) for 0.1 % iso-octane at φ =1.5. Experiments are from [32]. See digital paper for color version of this figure.

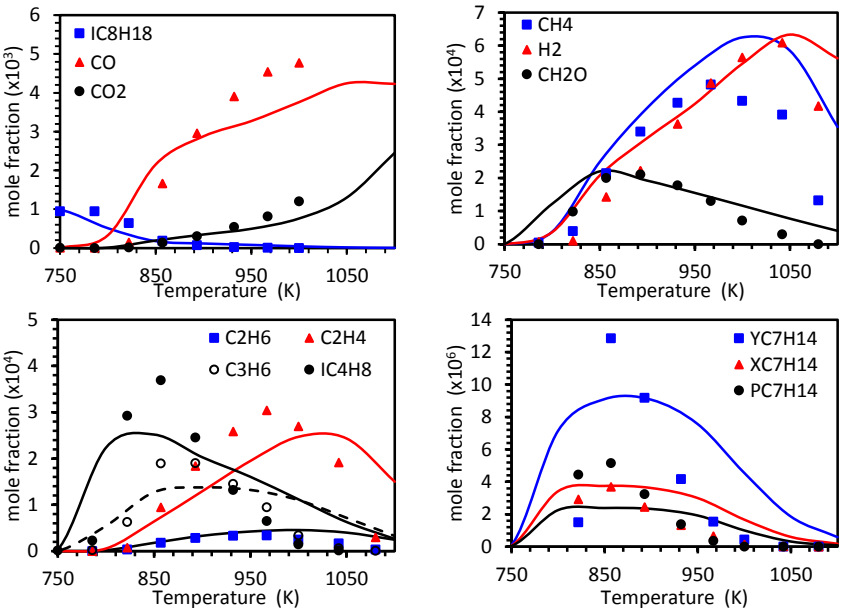

Figure 19. JSR species concentration profiles (points) and simulations using updated model (straight lines) and original model [1] (dashed lines) for 0.1 % iso-octane at φ =1.0. Experiments are from [32]. See digital paper for color version of this figure.

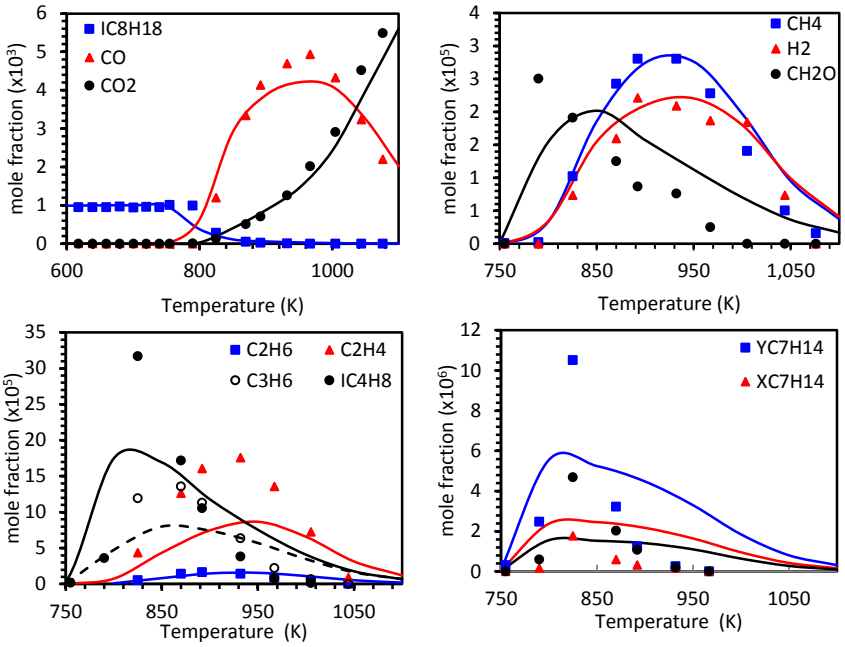

Figure 20. JSR species concentration profiles (points) and simulations using updated model (straight lines) and original model [1] (dashed lines) for 0.1 % iso-octane at φ =0.5. Experiments are from [32]. See digital paper for color version of this figure.

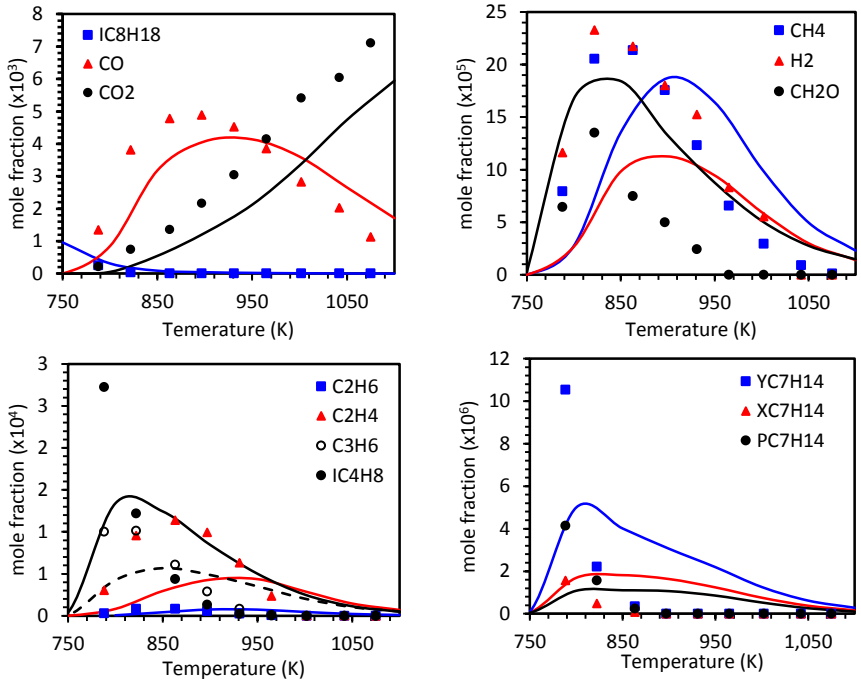

Figure 21. JSR species concentration profiles (points) and simulations using updated model (straight lines) and original model [1] (dashed lines) for 0.1 % iso-octane at φ =0.3. Experiments are from [32]. See digital paper for color version of this figure.

4-2-3 Laminar Flame Speed

In addition to IDT measurements, the updated model was tested against laminar flame speed data available in the literature carried out at atmospheric pressure [21, 24-26, 28, 29] and high pressure [23]. Flame speeds depend strongly on the base chemistry; however, different fuels produce different concentrations of C_1-C_4 species and this impacts the flame speed. In their analysis, Ji et al. [29] showed that a high concentration of iso-butene is produced during the oxidation of iso-octane, mainly from the β-scission of iso-octyl radicals, which affects its flame speed. To minimize computational time and cost, the proposed updated mechanism was reduced and only high temperature reaction pathways were retained.

The model was reduced using the method of direct relation graph with expert knowledge (DRG-X) [87]. This approach assumes that some species are weakly coupled to others, so they do not play a significant role in combustion processes, and as such, they can be removed whilst retaining the chemical fidelity of the remaining species. Also, contrary to the original DRG approach that is restricted by a uniform error tolerance for all the species, the DRG-X method allows a separate controlled reduction error for heat release rate and species of interest. Therefore, the DRG-X method can result in a smaller reduced mechanism with similar chemical fidelity compared to the original DRG method. In this work, the detailed mechanism is reduced by specifying the error tolerance for heat release as 0.01, for Ḣ atoms and ȮH radicals as 0.1, for iso-octane as 0.5, and for other species as 0.4. The target temperatures and pressures for the reduction are 1000-2300 K and 1-10 atm respectively. A skeletal mechanism with 189 species was generated from the detailed mechanism. The transport parameters for some species in the reduced model were estimated by analogy, except for the Lennard-Jones collision parameters that were estimated using critical temperature, critical pressure, and acentric factor properties based on Tee et al.'s [88] method. The reduced mechanism and the transport file are provided as Supplementary Material.

The simulations were carried out on CloudFlame [89-91], a cyber-infrastructure that presents a web front-end for Cantera [92]. The premixed laminar flame speed module was used with a domain size of 5 cm and a initial base grid of 20 points; the final solution exhibited grid-convergence with approximately 260 grid points. Figure 22 shows the experimental and simulation results for flame speeds measured at 1 atm and at 298 K and 353 K. Simulations show

good agreement with experimental data for fuel-lean conditions at both temperatures; however the model under predicts flame speeds at fuel-rich conditions at 298 K. In general, the model matches well with the experimental data at 355 K [24,29] across the entire range of equivalence ratios when considering the typical experimental uncertainty of ± 2 cm s^{-1}.

In addition, the model was used to simulate high pressure flame speed experiments carried out at 10 atm and temperatures of 323 K, 373 K, 423 K and 473 K with a high-speed shadowgraph system [23]. Figure 23 shows that the updated model agrees within the experimental uncertainty to the experimental data of [23] .

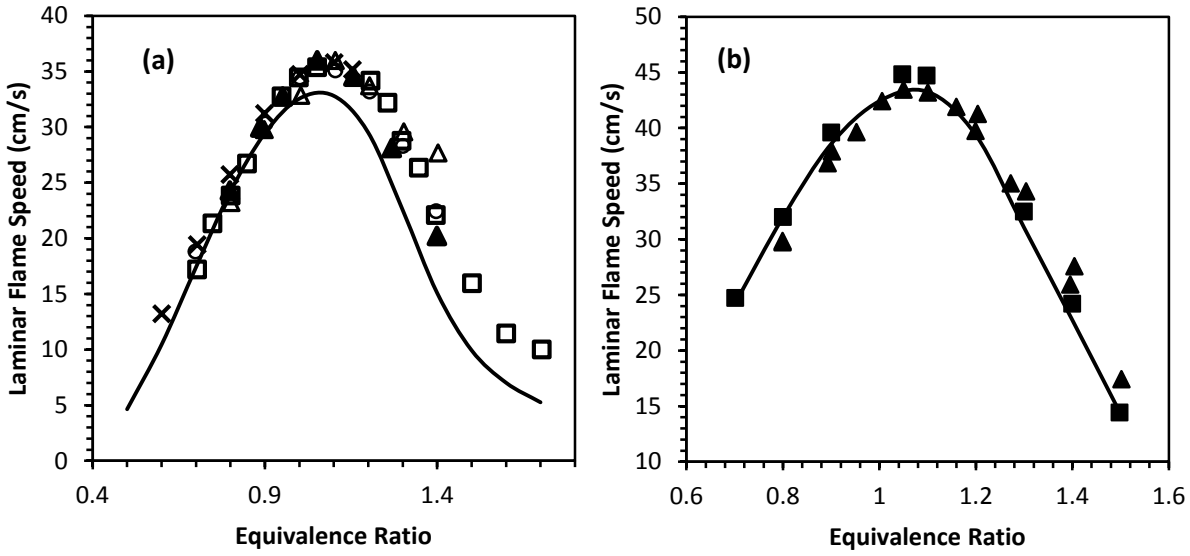

Figure 22. Iso-octane/air premixed laminar flame speeds at 1 atm and (a) 298 K and (b) 355 K. Experimental data (symbols) are given for open squares [21], closed triangles [24], crosses [25], open triangles [26], open circles [28], and closed squares [29]. Solid lines represent simulations using the updated model.

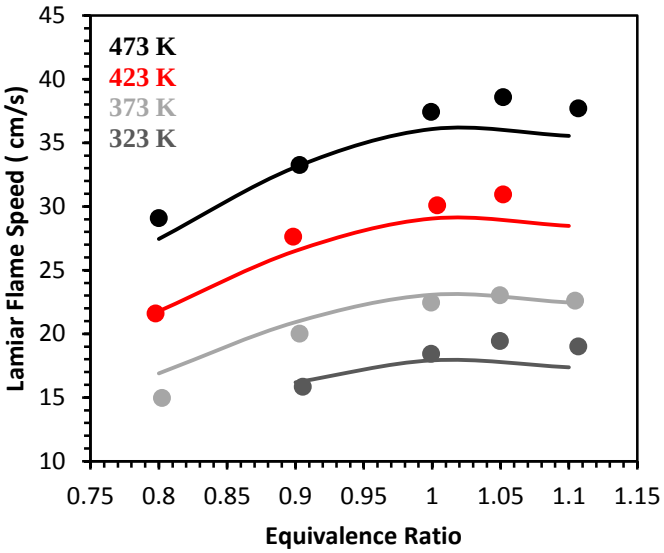

Figure 23. Iso-octane/aire premixed laminar flame speeds at 10 atm initial pressure and different initial temperatures. Experiments (symbols) are from [23]. Solid lines represent simulations using the updated model.See digital paper for color version of this figure.

4-2-4 Counterflow Diffusion Flame

Numerical simulations were also carried out to compare the skeletal model against ignition temperature measurements by [54] at different strain rates and iso-octane mass fractions. The experiment were carried out in counterflow diffusion flames. The fuel stream was comprised pre-vaporized isooctane in nitrogen diluent, while the oxidizer stream was air. Counterflow flame ignition simulations were performed using the OPPDIF solver in CHEMKIN-PRO [71]. A temperature profile was first established with cold mixtures at the oxidizer and fuel inlets, and then the temperature of the oxidizer stream was gradually raised until ignition. The composition of the fuel and the oxidizer streams and the temperature of the fuel stream, T1, were maintained constant while carrying out this procedure [93, 94]. The calculations were carried out with thermal diffusion, mixture-averaged transport and convergence parameters of GRAD = 0.25 and CURVATURE = 0.25. Overall, the model captured the trend in the experiment, with a maximimum 10 K difference observed in the ignition temperatures, as shown in Fig. 24.

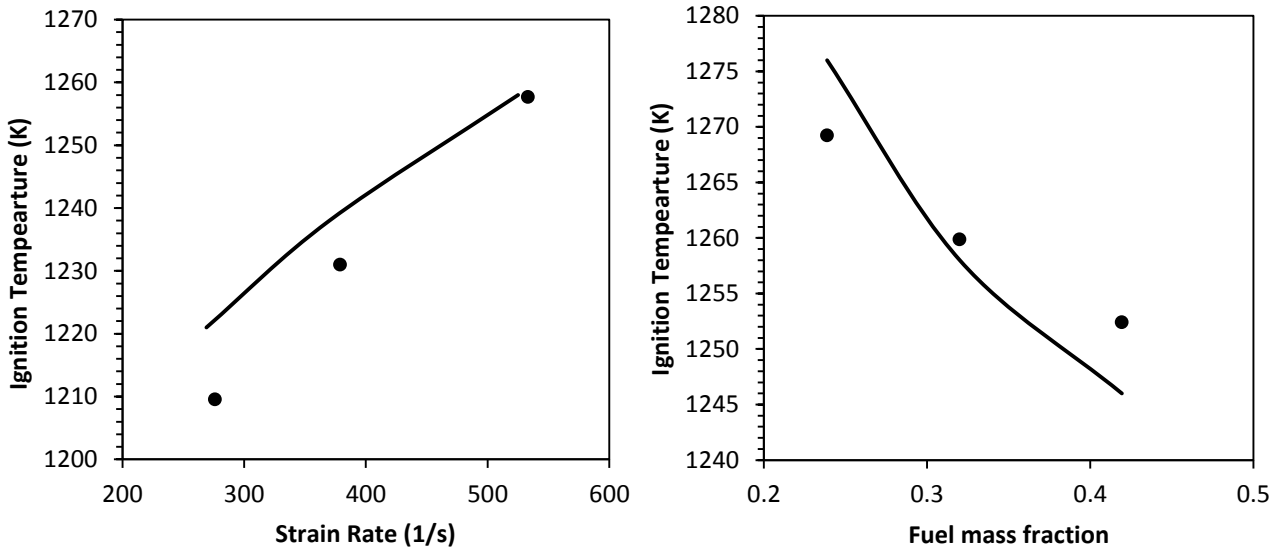

Figure 24. Iso-octane/air counterflow diffusion flame ignition temperature. Experiments (symbols) are from [23]. Solid lines represent simulations using the updated model.

4-2-5Pyrolysis in shock tube

The updated model was also tested against shock tube pyrolysis experiments from Malewicki et al. [12]. Generally, pyrolysis mechanisms consist of unimolecular decomposition of fuel, *β*-scission, isomerization of alky radicals reactions and abstraction by CH_3. The first 3 reaction classes were not updated in this study even though these classes have been recently studied. Wang et al. [95] calculated the rate coefficients of radical isomerization reactions at the CBS-QB3 level of theory. Their calculated values are similar to those used in the original model [35] with a maximum difference in rate constants of 13% at 1200 K. The rates are compared in Fig. S13 in the Supplementary material. Meanwhile, the kinetics of unimolecular decomposition of iso-octane has been computationally studied by Ning et al. [44]. Their calculated rate constants are much higher than those of Tsang et al. [96] that are used in the original mechanism. Both sets of values have been tested against the experimental pyrolysis concentration profile of iso-octane measured by [12].

Malewicki et al. [12] conducted pyrolysis experiments for diluted iso-octane mixtures (137 ppm and 149 ppm) in argon at 25 atm and 50 atm, and at different reaction times over the temperature range of 900–1700 K in a high pressure shock tube. They measured the concentrations of stable species using gas chromatography. Figure 25 compares the experimental concentration profile of

iso-octane to those simulated using unimolecular decomposition rate constants from Tsang et al. [96] and from Ning et al. [44]. The figure clearly shows that the Tsang et al.'s [96] values are needed in order for the model to match the experimental profile. Therefore, Tsang et al.'s values were retained in the updated mechanism.

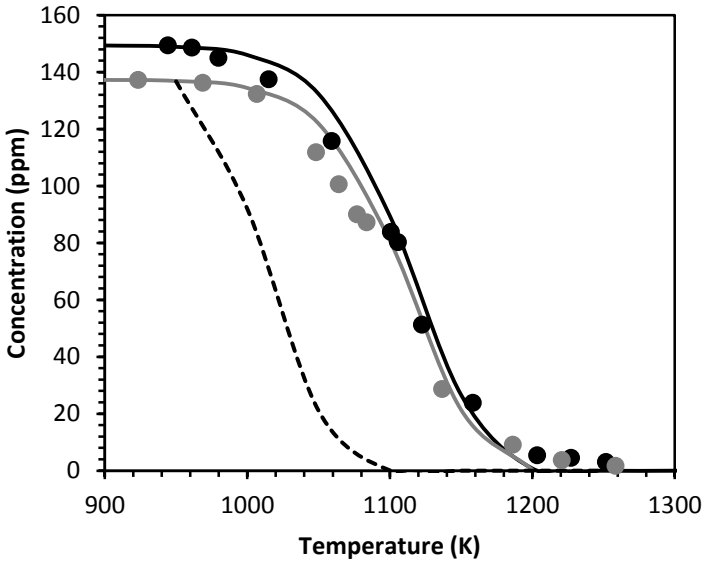

Figure 25. Experimental [12] (symbols) and simulated (lines) concentration profiles of iso-octane pyrolysis at 25 atm (grey) and 50 atm (black). Solid and dashed line represents simulations using unimolecular decomposition rates from [96]and [44], respectively.

Figure 26 shows the concentration profiles of the major measured species at 25 atm and 50 atm. The model matches the experimental concentration profiles of all detected species, except for those of acetylene (C_2H_2) and methane (CH_4), which are over-predicted and under-predicted, respectively.

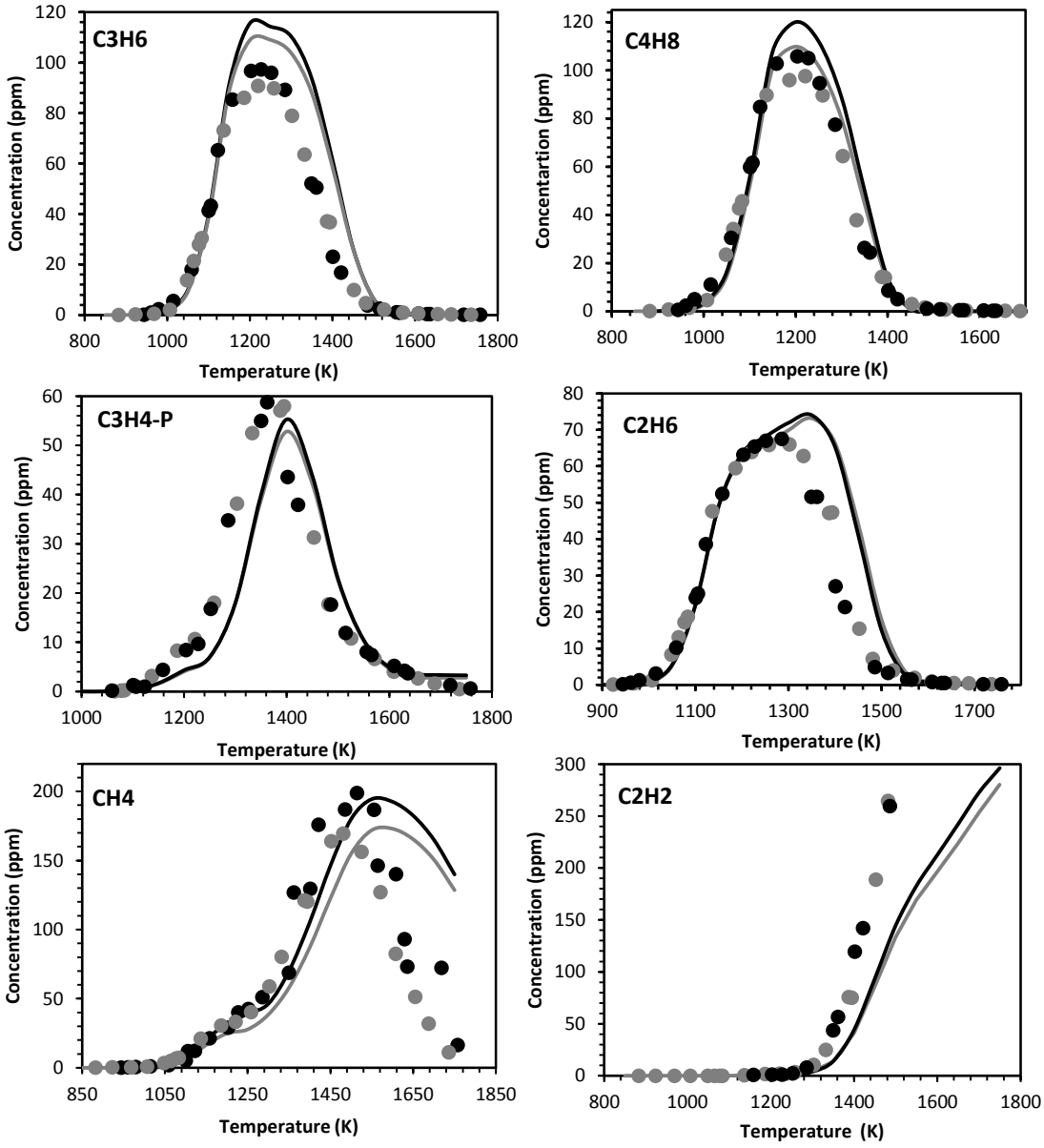

Figure 26. Concentration profiles of propene (C_3H_6), iso-butene+1-butene (C_4H_8), propyne (C_3H_4-P), ethane (C_2H_6), methane (CH_4) and acetylene (C_2H_2) produced from iso-octane pyrolysis at 25 atm (grey) and 50 atm (black). Symbols and lines represent experiments and simulations, respectively.

4-3 Sensitivity Analyses

In order to elucidate the reactions responsible for iso-octane ignition under different conditions, brute force sensitivity analyses were carried out using CHEMKIN-PRO [71] for stoichiometric iso-octane/air mixtures at 20 atm and at 650 K, 750 K and 850 K.

First, $\dot{O}H$ and $H\dot{O}_2$ radicals sensitivity analyses were performed at each condition to identify reactions that should be considered for brute force sensitivity analysis. The sensitivity coefficient of every reaction, at each temperature condition, was then calculated using the following equation:

$$\sigma = \frac{\log(\frac{\tau_2}{\tau_{0.5}})}{\log(\frac{2}{0.5})}$$

where τ_2 and $\tau_{0.5}$ are the ignition delay times computed with rate constant multiplied and divided by a factor of two, respectively. A positive sensitivity coefficient (σ) indicates that the specified reaction increases the simulated ignition delay time, and thus, decreases reactivity, and vice versa. Plots of $\dot{O}H$ and $H\dot{O}_2$ radicals sensitivity analyses are available as Supplementary Material, Figs. S14–S19. The figures demonstrates that, both analyses show the same important reactions.

Figure 27 shows the results of the brute force sensitivity analyses at 650, 750 and 850 K. At all the considered temperatures, the ignition delay time is most sensitive to rates of H-atom abstraction by $\dot{O}H$ radicals. However, abstractions from primary ($A\dot{C}_8H_{17}$ and $D\dot{C}_8H_{17}$) and secondary ($B\dot{C}_8H_{17}$) sites increase reactivity, whereas abstractions from the tertiary site ($C\dot{C}_8H_{17}$) decreases reactivity due to the lack of low-temperature chain-branching paths from this site and the production of relatively unreactive olefins, as will be discussed in the next section. The sensitivity analysis also shows that the rate of H-atom abstraction from the secondary site by $H\dot{O}_2$ radicals is more important than $\dot{O}H$ radicals only at 850K, where the high activation barrier of H-atom abstraction by $H\dot{O}_2$ radicals is overcome.

The isomerization of $AC_8H_{17}\dot{O}_2$ to $A\dot{C}_8H_{16}$OOH-C has negative effect on sensitivity because these reactions compete with the formation of $A\dot{C}_8H_{16}$OOH-B with which addition to O_2 is very promoting (Fig. 27). Also the formation of H_2O_2 molecules from $H\dot{O}_2$ radical self-reaction exhibits a positive sensitivity, as this is a chain termination step where $H\dot{O}_2$ radicals form two stable species.

The formation of cyclic ethers from hydroperoxy alkyl radicals (QOOH) exhibits a positive sensitivity coefficient at all temperatures while its competing pathway; addition to O_2 (second O_2

addition) shows a negative sensitivity coefficient . The effect of both classes is more significant at 750 K (NTC region). Moreover, the rates of production of hydroperoxy cyclic ethers (e.g. D(OOH)ETRBD, Fig. 27) and 3rd addition to O_2 (e.g. C8(OOH)BD-DO_2) showed a positive and negative sensitivity for the low temperature case (650 K), respectively. The appearance of these rates in the sensitivity analysis manifests the importance of these added pathways.

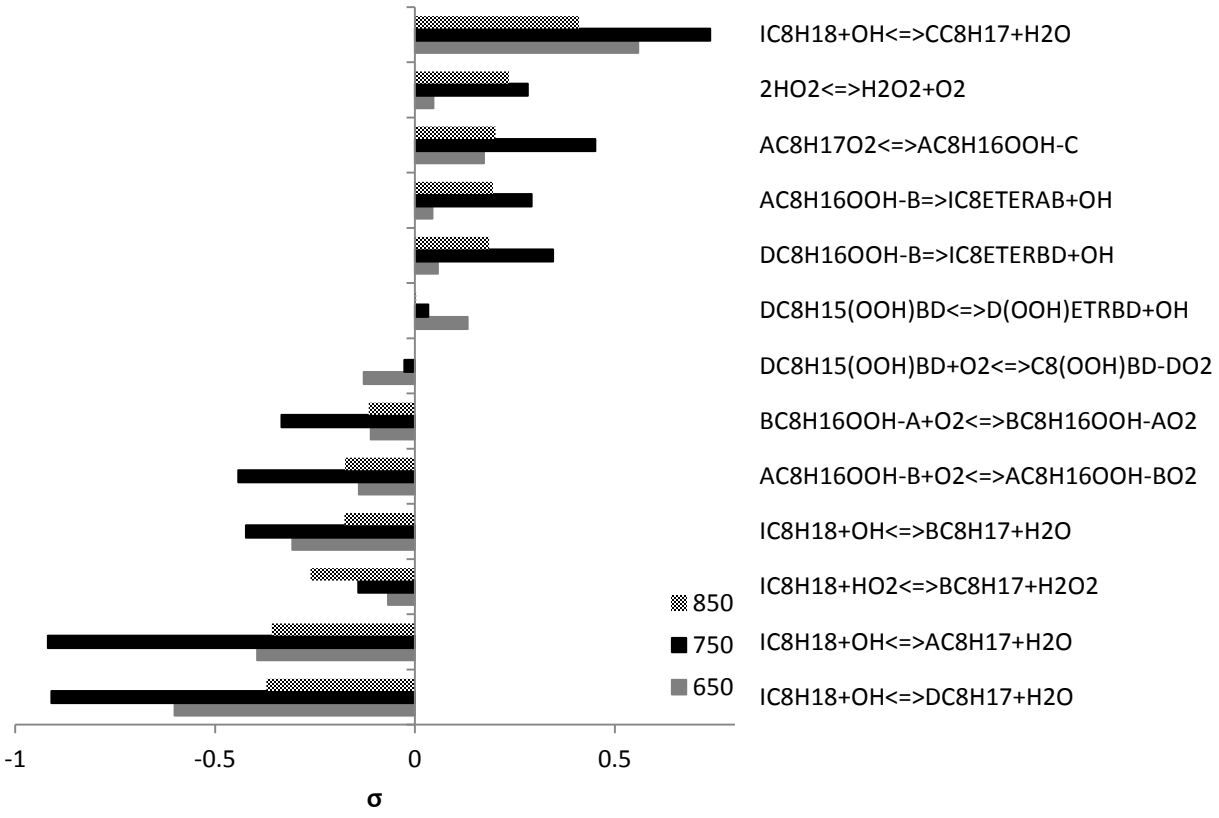

Figure 27. Brute force sensitivity analyses for ignition delay of stoichiometric iso-octane/air mixtures at 20 atm and different temperatures. (See Supplementary Material for species dictionary)

4-4 Rate of production analysis

Rate of production (ROP) analysis for stoichiometric iso-octane/air mixture at 20 atm, 750 K, and 20% fuel conversion is presented in Fig. 28. The ROP demonstrates that the major radical produced from iso-octane is $A\dot{C}_8H_{17}$ due to the presence of nine equivalent hydrogen atoms at this site. Also the figure shows that the predominant pathway for alkyl radicals at 750 K is addition to molecular oxygen. Once the alkylperoxy radical is formed, it either undergoes

concerted elimination to form an olefin + $H\dot{O}_2$ radical or it isomerizes to hydroperoxy alkyl (QOOH) radicals. For example, 98 % of the formed tertiary peroxy radical ($C\dot{C}_8H_{17}$) follows the concerted elimination pathway, which agrees with the findings of Snitsiriwat and Bozzelli [43], who argued that the main product of the tertiary iso-octyl radical + O_2 system is iso-octene + $H\dot{O}_2$. The concerted elimination chain termination pathway of the tertiary peroxy radical is favored by the absence of 6-membered ring isomerization pathways. Hence the production of tertiary iso-octyl radicals inhibits reactivity. On the other hand, $DC_8H_{17}\dot{O}_2$, a primary iso-octyl peroxy radical, produces two different hydroperoxy alkyl radicals through 6-membered ring transition states, which are more favorable than concerted elimination due to the lower ring strain. The other primary iso-octyl peroxy radical, $AC_8H_{17}\dot{O}_2$, does not undergo concerted elimination due to the absence of beta hydrogens, and rather undergoes isomerization reactions involving six-membered ring transition states that lead to low temperature chain-branching and promote reactivity.

None of the hydroperoxy alkyl radicals (QOOH) shown in Fig. 28 are *β*-QOOH radicals, therefore, the primary consumption pathways are: formation of cyclic ethers and addition to O_2. In general, the pathway forming cyclic ethers shows a higher flux than addition to O_2 due to the low thermodynamic stability of the ȮOQOOH radicals. Once formed at the relatively high temperature investigated, they favor back dissociation to O_2 and QOOH. RO_2 isomerizations involving seven-membered ring transition states often lead to cyclic ether formation rather than low-temperature chain branching because these isomerizations have lower rate constants than those involving six-membered rings that lead to chain branching. This behavior is evident for the seven-membered ring RO_2 isomerization leading to $A\dot{C}_8H_{16}$OOH-C radicals (98% of these radicals form the cyclic ether (IC_8ETERAC)).

Figure 28 also shows the ROP of different species from the original model [1], which highlights the mechanisitic difference between both models. Generally, the rate of consumption of IC_8H_{18} is lower using the original model when compared to the updated one, as previously demonstrated by the JSR profiles (Figs. S8-S11). The original model shows a higher flux going to $C\dot{C}_8H_{17}$ compared to $B\dot{C}_8H_{17,}$ which contradicts the updated model. The updated model has different branching ratios due to the implementation of updated iso-octane+OH abstraction rates that account for NNN effects. Moreover, the original model shows that addition to O_2 is favored by the alkyl radicals except for $C\dot{C}_8H_{17}$ where β-scission is more favored. This is attributed to the

absence of consumption pathways for the peroxy-hydroperoxy alkyls (ȮOQOOH) with a tertiary hydroperoxy group, which prevents the initial tertiary radical from contributing towards radical chain branching.

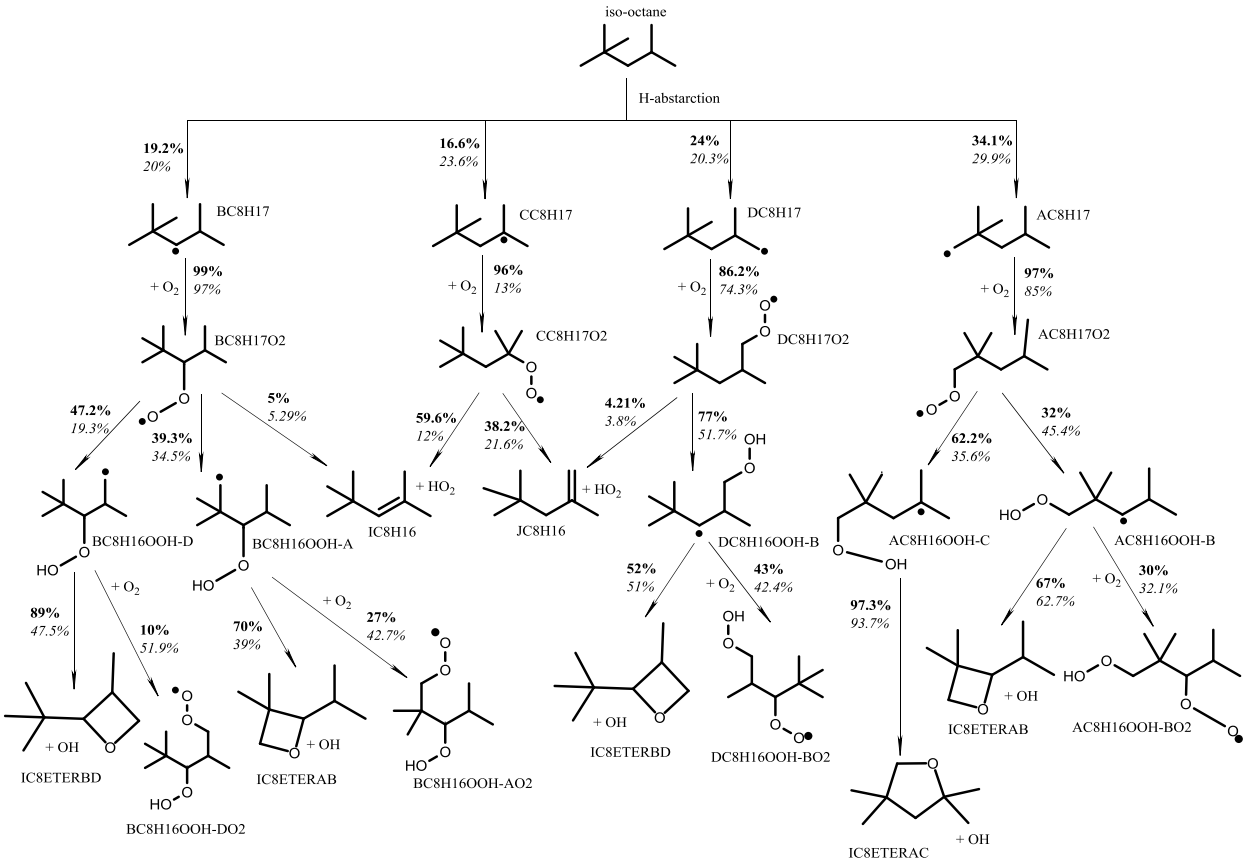

Figure 28. ROP analysis for stoichiometric iso-octane/air mixture at 20 atm-750 K and 20% fuel consumption corresponding to 788 K for the updated model in **bold** and 791 K for original model [1] in *italic*.

4-5 Effect of Alternative Isomerization and 3rd O_2 Addition Pathways on Reactivity

Including the alternative isomerization pathway in the mechanism required the addition of 206 reactions and 100 new species to the model. Figure 29 demonstrates that the addition of this pathway increased the reactivity of the mechanism at low temperature and NTC. This agrees with the findings of Silke et al. [70] and Mohamed et al. [51] for *n*-heptane and 2-methylhexane models, respectively. These findings encourage more thorough investigation of other low temperature oxidation pathways, which may be relevant to combustion kinetic models.

Peroxy-hydroperoxy alkyls (ȮOQOOH) with a tertiary hydroperoxy group do not form KHPs due to absence of α-hydrogen atoms. In the original mechanism, these species were accumulated in the system, but in the current model they form alkyl-dihydroperoxides ($P(OOH)_2$).

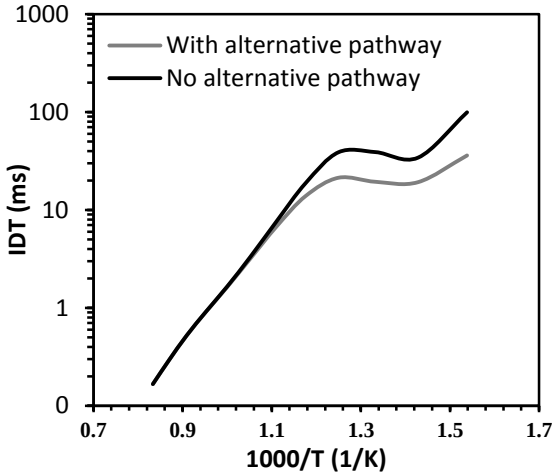

Figure 29. Ignition delay simulation at 20 atm and φ = 1.0 presented to demonstrate the effect of alternative isomerization pathways.

To better understand the importance of the added pathways, ROP analyses were performed for the 3 $P(OOH)_2$ radical with the highest concentrations at a pressure of 20 atm, equivalence ratio of 1 , and temperatures of 650 K and 750 K , where 650 K shows behavior in the low temperature region and 750 K in the middle of the NTC region. The analyses were conducted at 20% of fuel consumption for each case and results are shown in Fig.30.

Figure 30 shows that the formation of alkyl-dihydroperoxides from ȮOQOOH radicals may be more important than the formation of KHPs, depending on the size of the transition state rings. Alternative isomerization pathways with 6-membered ring transition states are the most favored due to lower ring strain energy compared to other isomerization reactions. However, in cases where the migrating hydrogen atom is at a tertiary site, the 7- membered ring transition state isomerization is more favorable than the 6-membered ring one that migrates an H-atom from the primary site, based on the reaction rate rules assigned in Section 2-3. For example, in Fig. 30-a , at 750 K, 51% of $BC_8H_{16}OOH\text{-}A\dot{O}_2$ forms $CC_8H_{15}(OOH)AB$ via a 7-membered ring transition state compared to 28 % for the formation of $AC_8H_{15}(OOH)AB$ via a 6-membered ring transition state.

Figure 30 also shows that the reactivity of ȮOQOOH species at low and intermediate temperatures are very similar. However, temperature-dependent variations in ROP are observed for $P(OOH)_2$ species. The third O_2 addition reactions are more favorable at low temperatures. For example, 44% of AC_8H_{15}(OOH)BD (Fig. 30(a)) undergoes 3rd O_2 addition at 650 K compared to 13.3% at 750 K. Similarly, 24.6% and 59.4% of DC_8H_{15}(OOH)BD (Fig. 30-a) and AC_8H_{15}(OOH)AB (Fig. 30-b) species undergo 3rd O_2 addition at 650 K compared to 4.55% and 13.1% at 750 K, respectively. It is notable that for the added alternative isomerization pathways both hydroperoxy cyclic ether (HPCE) formation and 3rd O_2 addition followed by formation of ketodihydroperoxides (KDHP) are chain branching pathways.

Although $H\dot{O}_2$ radical elimination reactions from $P(OOH)_2$ species have been added to the model, they do not affect reactivity as shown in Fig. 30. For iso-octane, hydroperoxy olefins may only be produced from $P(OOH)_2$ species via 5-membered ring transition states that are energetically un-favored.

Figure 30 also shows that the H-transfer from the hydroperoxy group attached to a primary site to the peroxy group attached to a secondary site via H-exchange pathway is more favorable than the opposite direction.

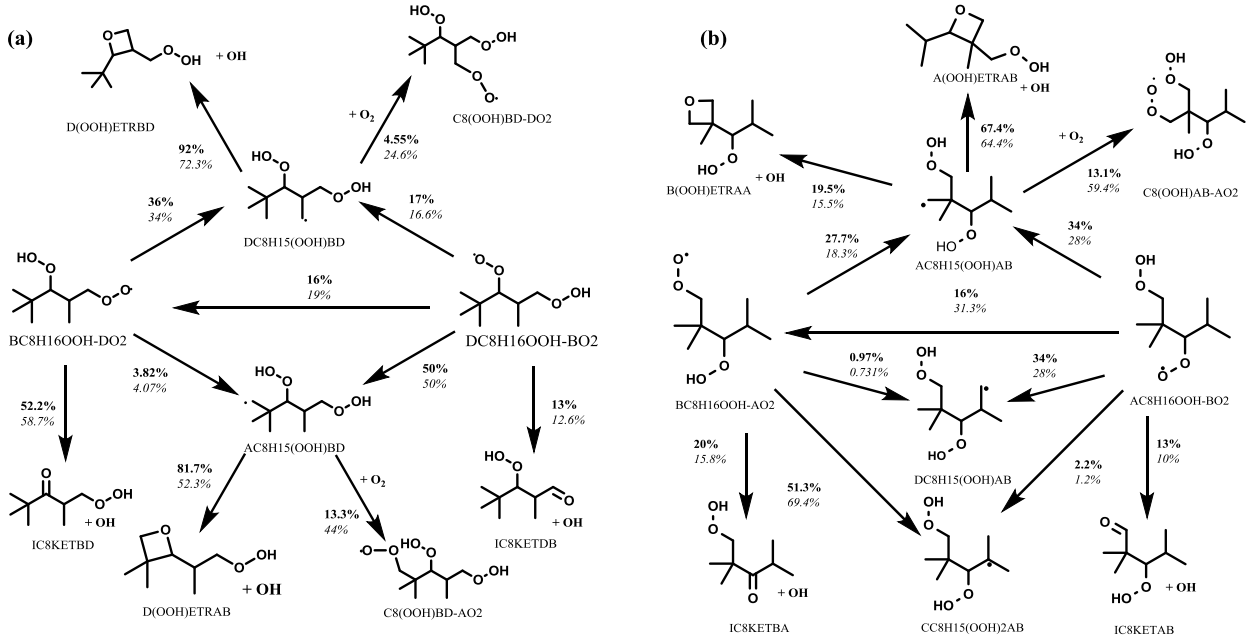

Figure 30. Flux analysis for alkyl-dihyroperoxides with the OOH on the (a) B-D sites and (b) A-B sites for stoichiometric iso-octane/air mixture at 20 atm at 20% fuel consumption. Values in

italic and **bold** represent ROP percentages at 650 K (Low temperature region) and 750 K (NTC region), respectively.

5- Conclusions

This paper presents a comprehensive chemical kinetic model for iso-octane, an important gasoline primary reference fuel surrogate. The iso-octane thermochemistry and mechanism were thoroughly updated using newly evaluated group values, reaction pathways, and rate rules. An alternative pathway for the isomerization of peroxy-alkyl hydroperoxides (ȮOQOOH) was included in the updated model along with 3rd O_2 addition reactions. The new model was compared against new rapid compression machine and high pressure shock tube experiments. The new experiments covered a range of temperatures and pressures that were not previously available in literature. Additional comparisons were presented against ignition delay, laminar flame speed, counterflow diffusion flame ignition, and speciation measurements available in the literature. The present model is compared against experimental data acquired across a temperature range of 630-1800K, pressure range of 10-50 atm, and equivalence ratio range of 0.25-2.

The present model shows improved agreement at lower equivalence ratios when compared to other mechanisms available in literature. Thus, the present model is appropriate for simulating engine combustions modes operating at lean conditions, such as various low temperature combustion engines.

Sensitivity analysis showed that the model is highly sensitive to H-atom abstraction from fuel molecules by ȮH radical. Flux analysis showed that the main pathway available for tertiary iso-octyl peroxy radical is concerted elimination, and this decreases the reactivity. The importance of the additional reaction pathways was also investigated. The addition of alternative isomerization increases the model reactivity, as all subsequent reaction pathways result in chain branching. The 3rd O_2 addition reaction pathway was shown to be more important at lower temperatures. These findings on the significance of new reaction pathways highlight the need for theoretical and experimental investigations of low temperature oxidation mechanisms. Indeed, the kinetic model presented here only represents the current state of knowledge on alkane auto-oxidation, and reaction pathways that are currently unexplored are not included in the model.

The rigorous and comprehensive kinetic model for iso-octane developed herein indicates that more fundamental research is needed to improve predictive capabilities. The thermochemistry of low temperature species derived from highly branched alkanes (e.g., iso-octane) need to be determined using computational chemistry at a high level of theory. This will facilitate the extrapolation of group values and correction parameters to account for various intra-molecular interactions (e.g., gauche and 1,5-interactions). Rate rules for highly branched alkanes also need to be determined using rigorous computational methods. Specifically, the rates for cyclic ether formation, alternative isomerization reactions, and 3rd addition to O_2 reactions require attention. Finally, kinetic model optimization with uncertainty quantification [97] can be used to improve the iso-octane model's predictions of combustion across a broad range of conditions.

Acknowledgement

The authors are grateful of insightful scientific discussions with Dr. Zhandong Wang (KAUST), Dr. Kuiwen Zhang (NUIG), Dr. John Bugler (NUIG), and Dr. Jihad Badra (Saudi Aramco). The presented work was supported by Saudi Aramco under the FUELCOM program and by the King Abdullah University of Science and Technology (KAUST) with competitive research funding given to the Clean Combustion Research Center (CCRC). The work at UCONN was supported by the National Science Foundation under Grant No. CBET-1402231. The work at LLNL was supported by the U.S. Department of Energy, Vehicle Technologies Office, program managers Gurpreet Singh and Leo Breton and was performed under the auspices of the U.S. Department of Energy by Lawrence Livermore National Laboratories under contract DE-AC52-07NA27344

References

[1] M. Mehl, W.J. Pitz, C.K. Westbrook, H.J. Curran, Kinetic modeling of gasoline surrogate components and mixtures under engine conditions, Proceedings of the Combustion Institute 33 (2011) 193-200.
[2] G.T. Kalghatgi, L. Hildingsson, A.J. Harrison, B. Johansson, Autoignition quality of gasoline fuels in partially premixed combustion in diesel engines, Proceedings of the combustion institute 33 (2011) 3015-3021.
[3] M.P.B. Musculus, P.C. Miles, L.M. Pickett, Conceptual models for partially premixed low-temperature diesel combustion, Progress in Energy and Combustion Science 39 (2013) 246-283.

[4] S. Saxena, I.D. Bedoya, Fundamental phenomena affecting low temperature combustion and HCCI engines, high load limits and strategies for extending these limits, Progress in Energy and Combustion Science 39 (2013) 457-488.
[5] J.E. Dec, Advanced compression-ignition engines—understanding the in-cylinder processes, Proceedings of the Combustion Institute 32 (2009) 2727-2742.
[6] M.A. Oehlschlaeger, D.F. Davidson, J.T. Herbon, R.K. Hanson, Shock tube measurements of branched alkane ignition times and OH concentration time histories, International Journal of Chemical Kinetics 36 (2004) 67-78.
[7] D.F. Davidson, B.M. Gauthier, R.K. Hanson, Shock tube ignition measurements of iso-octane/air and toluene/air at high pressures, Proceedings of the Combustion Institute 30 (2005) 1175-1182.
[8] H.-P.S. Shen, J. Vanderover, M.A. Oehlschlaeger, A shock tube study of iso-octane ignition at elevated pressures: The influence of diluent gases, Combustion and Flame 155 (2008) 739-755.
[9] M. Hartmann, I. Gushterova, M. Fikri, C. Schulz, R. Schießl, U. Maas, Auto-ignition of toluene-doped n-heptane and iso-octane/air mixtures: High-pressure shock-tube experiments and kinetics modeling, Combustion and Flame 158 (2011) 172-178.
[10] K. Fieweger, R. Blumenthal, G. Adomeit, Self-ignition of S.I. engine model fuels: A shock tube investigation at high pressure, Combustion and Flame 109 (1997) 599-619.
[11] K. Fieweger, R. Blumenthal, G. Adomeit, Twenty-Fifth Symposium (International) on CombustionShock-tube investigations on the self-ignition of hydrocarbon-air mixtures at high pressures, Symposium (International) on Combustion 25 (1994) 1579-1585.
[12] T. Malewicki, A. Comandini, K. Brezinsky, Experimental and modeling study on the pyrolysis and oxidation of iso-octane, Proceedings of the Combustion Institute 34 (2013) 353-360.
[13] A. Cox, J.F. Griffiths, C. Mohamed, H.J. Curran, W.J. Pitz, C.K. Westbrook. Extents of alkane combustion during rapid compression leading to single-and two-stage ignition. Symposium (International) on Combustion 26 (1996) 2685-2692.

[14] J.F. Griffiths, P.A. Halford-Maw, D.J. Rose, Fundamental features of hydrocarbon autoignition in a rapid compression machine, Combustion and flame 95 (1993) 291-306.

[15] C.V. Callahan, T.J. Held, F.L. Dryer, R. Minetti, M. Ribaucour, L.R. Sochet, T. Faravelli, P. Gaffuri, E. Rani. Experimental data and kinetic modeling of primary reference fuel mixtures. Symposium (International) on Combustion 26 (1996) 739-764.

[16] R. Minetti, M. Carlier, M. Ribaucour, E. Therssen, L.R. Sochet. Comparison of oxidation and autoignition of the two primary reference fuels by rapid compression. Symposium (International) on Combustion 26 (1996) 739-764

[17] R. Minetti, M. Ribaucour, M. Carlier, L.R. Sochet, Autoignition delays of a series of linear and branched chain alkanes in the intermediate range of temperature, Combustion science and technology 113 (1996) 747-753.

[18] X. He, M.T. Donovan, B.T. Zigler, T.R. Palmer, S.M. Walton, M.S. Wooldridge, A. Atreya, An experimental and modeling study of iso-octane ignition delay times under homogeneous charge compression ignition conditions, Combustion and Flame 142 (2005) 266-275.

[19] X. He, B.T. Zigler, S.M. Walton, M.S. Wooldridge, A. Atreya, A rapid compression facility study of OH time histories during iso-octane ignition, Combustion and flame 145 (2006) 552-570.
[20] S.M. Walton, X. He, B.T. Zigler, M.S. Wooldridge, A. Atreya, An experimental investigation of iso-octane ignition phenomena, Combustion and Flame 150 (2007) 246-262.
[21] S.G. Davis, C.K. Law, Laminar flame speeds and oxidation kinetics of iso-octane-air and n-heptane-air flames. Symposium (International) on Combustion 27 (1998) 521-527.

[22] D. Bradley, R.A. Hicks, M. Lawes, C.G.W. Sheppard, R. Woolley, The measurement of laminar burning velocities and Markstein numbers for iso-octane–air and iso-octane–n-heptane–air mixtures at elevated temperatures and pressures in an explosion bomb, Combustion and flame 115 (1998) 126-144.
[23] B. Galmiche, F. Halter, F. Foucher, Effects of high pressure, high temperature and dilution on laminar burning velocities and Markstein lengths of iso-octane/air mixtures, Combustion and Flame 159 (2012) 3286-3299.
[24] A.P. Kelley, W. Liu, Y.X. Xin, A.J. Smallbone, C.K. Law, Laminar flame speeds, non-premixed stagnation ignition, and reduced mechanisms in the oxidation of iso-octane, Proceedings of the Combustion Institute 33 (2011) 501-508.
[25] J.P.J. Van Lipzig, E.J.K. Nilsson, L.P.H. De Goey, A.A. Konnov, Laminar burning velocities of n-heptane, iso-octane, ethanol and their binary and tertiary mixtures, Fuel 90 (2011) 2773-2781.
[26] K. Kumar, J.E. Freeh, C.J. Sung, Y. Huang, Laminar flame speeds of preheated iso-octane/O_2/N_2 and n-heptane/O_2/N_2 mixtures, Journal of propulsion and power 23 (2007) 428-436.
[27] O.C. Kwon, M.I. Hassan, G.M. Faeth, Flame/stretch interactions of premixed fuel-vapor/O/N flames, Journal of Propulsion and Power 16 (2000) 513-522.
[28] Y. Huang, C.J. Sung, J.A. Eng, Laminar flame speeds of primary reference fuels and reformer gas mixtures, Combustion and Flame 139 (2004) 239-251.
[29] C. Ji, S.M. Sarathy, P.S. Veloo, C.K. Westbrook, F.N. Egolfopoulos, Effects of fuel branching on the propagation of octane isomers flames, Combustion and Flame 159 (2012) 1426-1436.
[30] N. Liu, S.M. Sarathy, C.K. Westbrook, F.N. Egolfopoulos, Ignition of non-premixed counterflow flames of octane and decane isomers, Proceedings of the Combustion Institute 34 (2013) 903-910.
[31] J.D. Blouch, C.K. Law, Non-premixed ignition of n-heptane and iso-octane in a laminar counterflow, Proceedings of the Combustion Institute 28 (2000) 1679-1686.
[32] P. Dagaut, M. Reuillon, M. Cathonnet, High Pressure Oxidation of Liquid Fuels From Low to High Temperature. 1. n-Heptane and iso-Octane, Combustion Science and Technology 95 (1993) 233-260.
[33] P.G. Lignola, F.P. Di Maio, A. Marzocchella, R. Mercogliano, E. Reverchon, JSFR combustion processes of n-heptane and isooctane, Symposium (International) on Combustion 22 (1989) 1625-1633.
[34] A. D'Anna, R. Mercoguano, R. Barbella, A. Ciajolo, Low temperature oxidation chemistry of iso-octane under high pressure conditions, Combustion science and technology 83 (1992) 217-232.
[35] H.J. Curran, P. Gaffuri, W.J. Pitz, C.K. Westbrook, A comprehensive modeling study of iso-octane oxidation, Combustion and Flame 129 (2002) 253-280.

[36] H.J. Curran, P. Gaffuri, W.J. Pitz, C.K. Westbrook, A Comprehensive Modeling Study of n-Heptane Oxidation, Combustion and Flame 114 (1998) 149-177.
[37] M. Mehl, W.J. Pitz, M. Sjöberg, J.E. Dec, Detailed Kinetic Modeling of Low-Temperature Heat Release for PRF Fuels in an HCCI Engine, Report No. 2009-01-1806, SAE International, Warrendale, PA, 2009.
[38] S.M. Sarathy, G. Kukkadapu, M. Mehl, W. Wang, T. Javed, S. Park, M.A. Oehlschlaeger, A. Farooq, W.J. Pitz, C.-J. Sung, Ignition of alkane-rich FACE gasoline fuels and their surrogate mixtures, Proceedings of the Combustion Institute 35 (2015) 249-257.
[39] D. Vuilleumier, H. Selim, R. Dibble, M. Sarathy, Exploration of heat release in a homogeneous charge compression ignition engine with primary reference fuels, SAE Technical Paper, 2013.
[40] W. Hwang, J. Dec, M. Sjöberg, Spectroscopic and chemical-kinetic analysis of the phases of HCCI autoignition and combustion for single-and two-stage ignition fuels, Combustion and Flame 154 (2008) 387-409.
[41] S. Snitsiriwat, J.W. Bozzelli, Thermochemical Properties for Isooctane and Carbon Radicals: Computational Study, The Journal of Physical Chemistry A 117 (2013) 421-429.
[42] I. Auzmendi-Murua, J.W. Bozzelli, Thermochemistry, Reaction Paths, and Kinetics on the Secondary Isooctane Radical Reaction with O_2, International Journal of Chemical Kinetics 46 (2014) 71-103.
[43] S. Snitsiriwat, J.W. Bozzelli, Thermochemistry, Reaction Paths, and Kinetics on the tert-Isooctane Radical Reaction with O_2, The Journal of Physical Chemistry A 118 (2014) 4631-4646.
[44] H. Ning, C. Gong, Z. Li, X. Li, Pressure-Dependent Kinetics of Initial Reactions in Iso-octane Pyrolysis, The Journal of Physical Chemistry A 119 (2015) 4093-4107.
[45] S.M. Villano, L.K. Huynh, H.-H. Carstensen, A.M. Dean, High-pressure rate rules for alkyl + O_2 reactions. 1. The dissociation, concerted elimination, and isomerization channels of the alkyl peroxy radical, The Journal of Physical Chemistry. A 115 (2011) 13425-13442.
[46] S.M. Villano, L.K. Huynh, H.H. Carstensen, A.M. Dean, High-pressure rate rules for alkyl + O_2 reactions. 2. The isomerization, cyclic ether formation, and beta-scission reactions of hydroperoxy alkyl radicals, J Phys Chem A 116 (2012) 5068-5089.
[47] A. Miyoshi, Systematic computational study on the unimolecular reactions of alkylperoxy (RO_2), hydroperoxyalkyl (QOOH), and hydroperoxyalkylperoxy (O2QOOH) radicals, The Journal of Physical Chemistry. A 115 (2011) 3301-3325.
[48] S. Sharma, S. Raman, W.H. Green, Intramolecular Hydrogen Migration in Alkylperoxy and Hydroperoxyalkylperoxy Radicals: Accurate Treatment of Hindered Rotors, The Journal of Physical Chemistry A 114 (2010) 5689-5701.
[49] J. Bugler, K.P. Somers, E.J. Silke, H.J. Curran, Revisiting the Kinetics and Thermodynamics of the Low-Temperature Oxidation Pathways of Alkanes: A Case Study of the Three Pentane Isomers, The Journal of Physical Chemistry. A 119 (2015) 7510-7527.
[50] K. Zhang, C. Banyon, C. Togbé, P. Dagaut, J. Bugler, H.J. Curran, An experimental and kinetic modeling study of n-hexane oxidation, Combustion and Flame 162 (2015) 4194-4207.
[51] S.Y. Mohamed, L. Cai, F. Khaled, C. Banyon, Z. Wang, M.J. Al Rashidi, H. Pitsch, H.J. Curran, A. Farooq, S.M. Sarathy, Modeling Ignition of a Heptane Isomer: Improved Thermodynamics, Reaction Pathways, Kinetics, and Rate Rule Optimizations for 2-Methylhexane, The Journal of Physical Chemistry A 120 (2016) 2201-2217.

[52] Z. Wang, L. Zhang, K. Moshammer, D.M. Popolan-Vaida, V.S.B. Shankar, A. Lucassen, C. Hemken, C.A. Taatjes, S.R. Leone, K. Kohse-Höinghaus, N. Hansen, P. Dagaut, S.M. Sarathy, Additional chain-branching pathways in the low-temperature oxidation of branched alkanes, Combustion and Flame 164 (2016) 386-396.
[53] Z. Wang, S.M. Sarathy, Third O2 addition reactions promote the low-temperature auto-ignition of n-alkanes, Combustion and Flame 165 (2016) 364-372.
[54] T. Bieleveld, A. Frassoldati, A. Cuoci, T. Faravelli, E. Ranzi, U. Niemann, K. Seshadri, Experimental and kinetic modeling study of combustion of gasoline, its surrogates and components in laminar non-premixed flows, Proceedings of the Combustion Institute 32 (2009) 493-500.
[55] W.B. Sidney, Thermochemical Kinetics: Methods for the Estimation of Thermochemical Data and Rate Parameters, 2 ed., John Wiley & Sons; 1976.
[56] E.R. Ritter, THERM: a computer code for estimating thermodynamic properties for species important to combustion and reaction modeling, J Chem Inf Comput Sci 31 (1991) 400-408.
[57] S.M. Burke, J.M. Simmie, H.J. Curran, Critical Evaluation of Thermochemical Properties of C1–C4 Species: Updated Group-Contributions to Estimate Thermochemical Properties, Journal of Physical and Chemical Reference Data 44 (2015) 013101.
[58] J.M. Simmie, K.P. Somers, Benchmarking Compound Methods (CBS-QB3, CBS-APNO, G3, G4, W1BD) against the Active Thermochemical Tables: A Litmus Test for Cost-Effective Molecular Formation Enthalpies, J Phys Chem A 119 (2015) 7235-7246.
[59] M.K. Sabbe, M. Saeys, M.-F. Reyniers, G.B. Marin, V. Van Speybroeck, M. Waroquier, Group Additive Values for the Gas Phase Standard Enthalpy of Formation of Hydrocarbons and Hydrocarbon Radicals, The Journal of Physical Chemistry A 109 (2005) 7466-7480.
[60] N. Cohen, S.W. Benson, Estimation of heats of formation of organic compounds by additivity methods, Chem. Rev. 93 (1993) 2419-2438.
[61] C.-W. Zhou, Y. Li, E. O'Connor, K.P. Somers, S. Thion, C. Keesee, O. Mathieu, E.L. Petersen, T.A. DeVerter, M.A. Oehlschlaeger, G. Kukkadapu, C.-J. Sung, M. Alrefae, F. Khaled, A. Farooq, P. Dirrenberger, P.-A. Glaude, F. Battin-Leclerc, J. Santner, Y. Ju, T. Held, F.M. Haas, F.L. Dryer, H.J. Curran, A comprehensive experimental and modeling study of isobutene oxidation, Combustion and Flame 167 (2016) 353-379.
[62] W.K. Metcalfe, W.J. Pitz, H.J. Curran, J.M. Simmie, C.K. Westbrook, The development of a detailed chemical kinetic mechanism for diisobutylene and comparison to shock tube ignition times, Proceedings of the Combustion Institute 31 I (2007) 377-384.
[63] S.M. Sarathy, C.K. Westbrook, M. Mehl, W.J. Pitz, C. Togbe, P. Dagaut, H. Wang, M.A. Oehlschlaeger, U. Niemann, K. Seshadri, P.S. Veloo, C. Ji, F.N. Egolfopoulos, T. Lu, Comprehensive chemical kinetic modeling of the oxidation of 2-methylalkanes from C7 to C20, Combustion and Flame 158 (2011) 2338-2357.
[64] R. Sivaramakrishnan, J.V. Michael, Rate constants for OH with selected large alkanes: Shock-tube measurements and an improved group scheme, Journal of Physical Chemistry A 113 (2009) 5047-5060.
[65] J. Badra, A. Farooq, Site-specific reaction rate constant measurements for various secondary and tertiary H-abstraction by OH radicals, Combustion and Flame 162 (2015) 2034-2044.
[66] N. Cohen, Are reaction rate coefficients additive? Revised transition state theory calculations for OH + alkane reactions, International Journal of Chemical Kinetics 23 (1991) 397-417.

[67] A. Miyoshi, Molecular size dependent falloff rate constants for the recombination reactions of alkyl radicals with O_2 and implications for simplified kinetics of alkylperoxy radicals, International Journal of Chemical Kinetics 44 (2012) 59-74.
[68] C.F. Goldsmith, W.H. Green, S.J. Klippenstein, Role of O_2 + QOOH in low-temperature ignition of propane. 1. Temperature and pressure dependent rate coefficients, The Journal of Physical Chemistry. A 116 (2012) 3325-3346.
[69] J. Bugler, B. Marks, O. Mathieu, R. Archuleta, A. Camou, C. Grégoire, K.A. Heufer, E.L. Petersen, H.J. Curran, An ignition delay time and chemical kinetic modeling study of the pentane isomers, Combustion and Flame 163 (2016) 138-156.
[70] E.J. Silke, H.J. Curran, J.M. Simmie, W.J. Pitz, C.K. Westbrook. A Rapid Compression Machine Modelling Study of the Heptane Isomers. European Combustion Meeting, Louvain-la-Neuve, Belgium (2005).

[71] R. Design, CHEMKIN-PRO, 15112; Reaction Design: San Diego, CA, 2011.

[72] G. Mittal, C.-J. Sung, A Rapid Compression Machine for Chemical Kinetics Studies at Elevated Pressures and Temperatures, Combustion Science and Technology 179 (2007) 497-530.
[73] A.K. Das, C.-J. Sung, Y. Zhang, G. Mittal, Ignition delay study of moist hydrogen/oxidizer mixtures using a rapid compression machine, International Journal of Hydrogen Energy 37 (2012) 6901-6911.
[74] J. Wurmel, J.M. Simmie, H.J. Curran, Studying the chemistry of HCCI in rapid compression machines, International journal of vehicle design 44 (2007) 84-106.
[75] W.S. Affleck, A. Thomas, An Opposed Piston Rapid Compression Machine for Preflame Reaction Studies, Proceedings of the Institution of Mechanical Engineers 183 (1968) 365-387.
[76] L. Brett, J. MacNamara, P. Musch, J.M. Simmie, Simulation of methane autoignition in a rapid compression machine with creviced pistons, Combustion and flame 124 (2001) 326-329.
[77] J. Würmel, E.J. Silke, H.J. Curran, M.S. Ó Conaire, J.M. Simmie, The effect of diluent gases on ignition delay times in the shock tube and in the rapid compression machine, Combustion and Flame 151 (2007) 289-302.
[78] J. Würmel, J.M. Simmie, CFD studies of a twin-piston rapid compression machine, Combustion and flame 141 (2005) 417-430.
[79] T. Lee, D. Mateescu, Experimental and numerical investigation of 2-d backward-facing step flow, Journal of Fluids and Structures 12 (1998) 703-716.
[80] S. Park, O. Mannaa, F. Khaled, R. Bougacha, M.S. Mansour, A. Farooq, S.H. Chung, S.M. Sarathy, A comprehensive experimental and modeling study of 2-methylbutanol combustion, Combustion and Flame 162 (2015) 2166-2176.
[81] Y. Uygun, S. Ishihara, H. Olivier, A high pressure ignition delay time study of 2-methylfuran and tetrahydrofuran in shock tubes, Combustion and Flame 161 (2014) 2519–2530.
[82] A.B. Mansfield, M.S. Wooldridge, H. Di, X. He, Low-temperature ignition behavior of iso-octane, Fuel 139 (2015) 79-86.
[83] S.W. Wagnon, M.S. Wooldridge, Effects of buffer gas composition on autoignition, Combustion and Flame 161 (2014) 898-907.
[84] S.M. Gallagher, H.J. Curran, W.K. Metcalfe, D. Healy, J.M. Simmie, G. Bourque, A rapid compression machine study of the oxidation of propane in the negative temperature coefficient regime, Combustion and Flame 153 (2008) 316-333.
[85] T. Javed, C. Lee, M. AlAbbad, K. Djebbi, M. Beshir, H. Curran, A. Farooq, Ignition studies of n-heptane/iso-octane/toluene blends, Combustion and Flame 171 (2016) 223–233.

[86] L. Cai, H. Pitsch, Optimized chemical mechanism for combustion of gasoline surrogate fuels, Combustion and Flame 162 (2015) 1623-1637.
[87] T. Lu, M. Plomer, Z. Luo, S.M. Sarathy, W.J. Pitz, S. Som, D.E. Longman, D.E. Longman, Directed Relation Graph with Expert Knowledge for Skeletal Mechanism Reduction, 7th US National Technical Meeting of the Combustion Institute Atlanta, GA, United States (2011).
[88] L.S. Tee, S. Gotoh, W.E. Stewart, Molecular Parameters for Normal Fluids. Lennard-Jones 12-6 Potential, Industrial and Engineering Chemistry Fundamentals 5 (1966) 356-363.
[89] N.N. G. Goteng, S.M. Sarathy, CloudFlame: Cyberinfrastructure for Combustion Research, IEEE, China, 2013.
[90] M.S. G.L. Goteng, N. Nettyam, A. Farooq, M. Frenklach, S.M. Sarathy, A Hybrid Cloud System for Combustion Kinetics Simulation, 23rd International Symposium on Gas Kinetics and Related Phenomena, Hungary, 2014.
[91] N.N. Zachary Reyno-Chiasson, Gokop L. Goteng, Matthew Speight,Bok Jik Lee, Sathya Baskaran, Jim Oreluk, Aamir Farooq, Hong G. Im, Michael Frenklach, S. Mani Sarathy, CloudFlame and PrIMe: accelerating combustion research in the cloud, 9th International Conference on Chemical Kinetics, Ghent, Belgium, 2015.
[92] Cantera: An Object-oriented Software Toolkit for Chemical Kinetics, Thermodynamics, and Transport Processes, 2016.
[93] A. Alfazazi, U. Niemann, H. Selim, R.J. Cattolica, S.M. Sarathy, Effects of substitution on counterflow ignition and extinction of C3 and C4 alcohols, Energy & Fuels 30 (2016) 6091-6097.
[94] S.M. Sarathy, U. Niemann, C. Yeung, R. Gehmlich, C.K. Westbrook, M. Plomer, Z. Luo, M. Mehl, W.J. Pitz, K. Seshadri, others, A counterflow diffusion flame study of branched octane isomers, Proceedings of the Combustion Institute 34 (2013) 1015-1023.
[95] K. Wang, S.M. Villano, A.M. Dean, Reactivity-Structure-Based Rate Estimation Rules for Alkyl Radical H Atom Shift and Alkenyl Radical Cycloaddition Reactions, The Journal of Physical Chemistry A ,119 (2015) 7205-7221.
[96] W. Tsang, Chemical Kinetic Data Base for Combustion Chemistry Part 4. Isobutane, Journal of Physical and Chemical Reference Data 19 (1990) 1-68.
[97] L. Cai, H. Pitsch, S.Y. Mohamed, V. Raman, J. Bugler, H.J. Curran, S.M. Sarathy, Optimized reaction mechanism rate rules for normal alkanes. , Combustion and Flame, (2016).